

Eight-color chiral spin liquid in the $S = 1$ bilinear-biquadratic model with Kitaev interactions

Rico Pohle,^{1,2} Nic Shannon,³ and Yukitoshi Motome²

¹*Graduate School of Science and Technology, Keio University, Yokohama 223-8522, Japan*

²*Department of Applied Physics, University of Tokyo, Hongo, Bunkyo-ku, Tokyo, 113-8656, Japan*

³*Theory of Quantum Matter Unit, Okinawa Institute of Science and Technology Graduate University, Onna-son, Okinawa 904-0412, Japan*

(Dated: August 6, 2024)

Multipolar spin systems provide a rich ground for the emergence of unexpected states of matter due to their enlarged spin degree of freedom. In this study, with a specific emphasis on $S = 1$ magnets, we explore the interplay between spin nematic states and spin liquids. Based on the foundations laid in the prior work [R. Pohle *et al.*, Phys. Rev. B **107**, L140403 (2023)], we investigate the $S = 1$ Kitaev model with bilinear-biquadratic interactions, which stabilizes, next to Kitaev spin liquid, spin nematic and triple- q phases, also an exotic chiral spin liquid. Through a systematic reduction of the spin degree of freedom – from \mathbb{CP}^2 to \mathbb{CP}^1 and ultimately to a discrete eight-color model – we provide an intuitive understanding of the nature and origin of this chiral spin liquid. We find that the chiral spin liquid is characterized by an extensive ground-state degeneracy, bound by a residual entropy, extremely short-ranged correlations, a nonzero scalar spin chirality marked by \mathbb{Z}_2 flux order, and a gapped continuum of excitations. Our work contributes not only to the specific exploration of $S = 1$ Kitaev magnets but also to the broader understanding of the importance of multipolar spin degree of freedom on the ground state and excitation properties in quantum magnets.

I. INTRODUCTION

Multipolar systems exhibit higher-order moments, such as quadrupoles and octupoles, even in absence of monopoles and dipoles. The inherent fluctuations and allowed higher-order interactions in these systems provide a rich landscape of unconventional phases, evident from multipolar order observed in quantum magnets [1–5], unconventional superconductors [6–11], and topological insulators [12, 13]. Particular exotic examples, including multipolar quantum spin ice [14–16], \mathbb{CP}^2 skyrmion crystals [17–19], and unconventional orders in the higher-spin Kondo lattice model [20, 21], demonstrate the diverse range of intriguing quantum phenomena present in multipolar condensed matter.

Multipolar magnets made of $S = 1$ moments are particularly intriguing, as they strike a delicate balance with a spin length that is “small enough” to exhibit strong quantum effects, while simultaneously being “large enough” to give rise to onsite quadrupole moments [22–25]. Quadrupoles break spin-rotation symmetry by selecting an axis without specifying a particular direction, closely resembling properties observed in classical liquid crystals [26–28]. This unique characteristic makes them an ideal playground for exploring topological defects [29, 30], investigating out-of-equilibrium effects [31, 32], and drawing potential analogies to gravity [33–35].

Despite being theoretically proposed almost 60 years ago [36, 37], the experimental exploration of $S = 1$ magnets has faced substantial challenges, primarily since their quadrupolar order remains hidden from conventional magnetic probes like neutron scattering [38, 39]. Fortunately, recent advancements in experimental techniques such as Raman scattering [40, 41], resonant inelastic X-ray scattering (RIXS) [42–44], and the exploration of physical properties like the magnetocaloric effect [45], combined with the development of powerful numerical techniques [46–51], have expanded our capabilities to interpret thermodynamic and dynamic properties of multipolar magnets in real materials. The successful application of these

diverse methods has significantly advanced our understanding of various $S = 1$ compounds, including NiGa_2S_4 [41, 52, 53], FeI_2 [54, 55], and $\text{Ba}_2\text{FeSi}_2\text{O}_7$ [56].

Recently, higher-spin Kitaev systems have attracted substantial attention [57–69], as they offer a new avenue for studying quantum spin liquids with potentially multipolar character [70, 71] and fractionalized excitations carrying multipolar moments [66]. Theoretical proposals suggest that magnets with strong Hund’s coupling and spin-orbit interactions could pave the way for experimental realizations [72], with promising candidate materials such as $\text{NaNi}_2\text{BiO}_{6-\delta}$ [73] and KNiAsO_4 [74]. Furthermore, $S = 1$ magnets naturally allow for higher-order interactions, such as biquadratic interactions, which effectively couple the quadrupole degree of freedom between individual spins.

In this context, the recent work by the authors explored the interplay between spin nematics and spin liquids in the $S = 1$ Kitaev model with bilinear-biquadratic (BBQ) interactions [75]. The richness of this model unfolds with a plethora of phases, including spin nematic, and Kitaev spin liquid states, alongside triple- q order with nonzero scalar spin chirality, ferro, antiferro, zigzag and stripy phases. Particularly intriguing is the presence of exotic phases where dipole and quadrupole moments compete. These include a quasi-one-dimensional coplanar phase, a twisted conical phase, and a noncoplanar ordered state. A comprehensive phase diagram showcasing these diverse phases is shown in Fig. 1(a).

Even though the model primarily stabilizes ordered phases in the ground state, it holds an intriguing surprise. In the vicinity of the noncoplanar ordered state, the model hosts an unconventional classical chiral spin liquid (CSL). This CSL exhibits an extensive degeneracy of states and retains the Kitaev spin liquid (SL) feature of \mathbb{Z}_2 flux order, along with a nonzero scalar spin chirality [75]. However, at a semiclassical level, this CSL does not appear in the ground state, as seen by its absence in Fig. 1(a). Instead, it is stabilized at finite temperatures, resisting magnetic dipolar order solely through thermal fluctuations, rather than quantum fluctuations or quantum en-

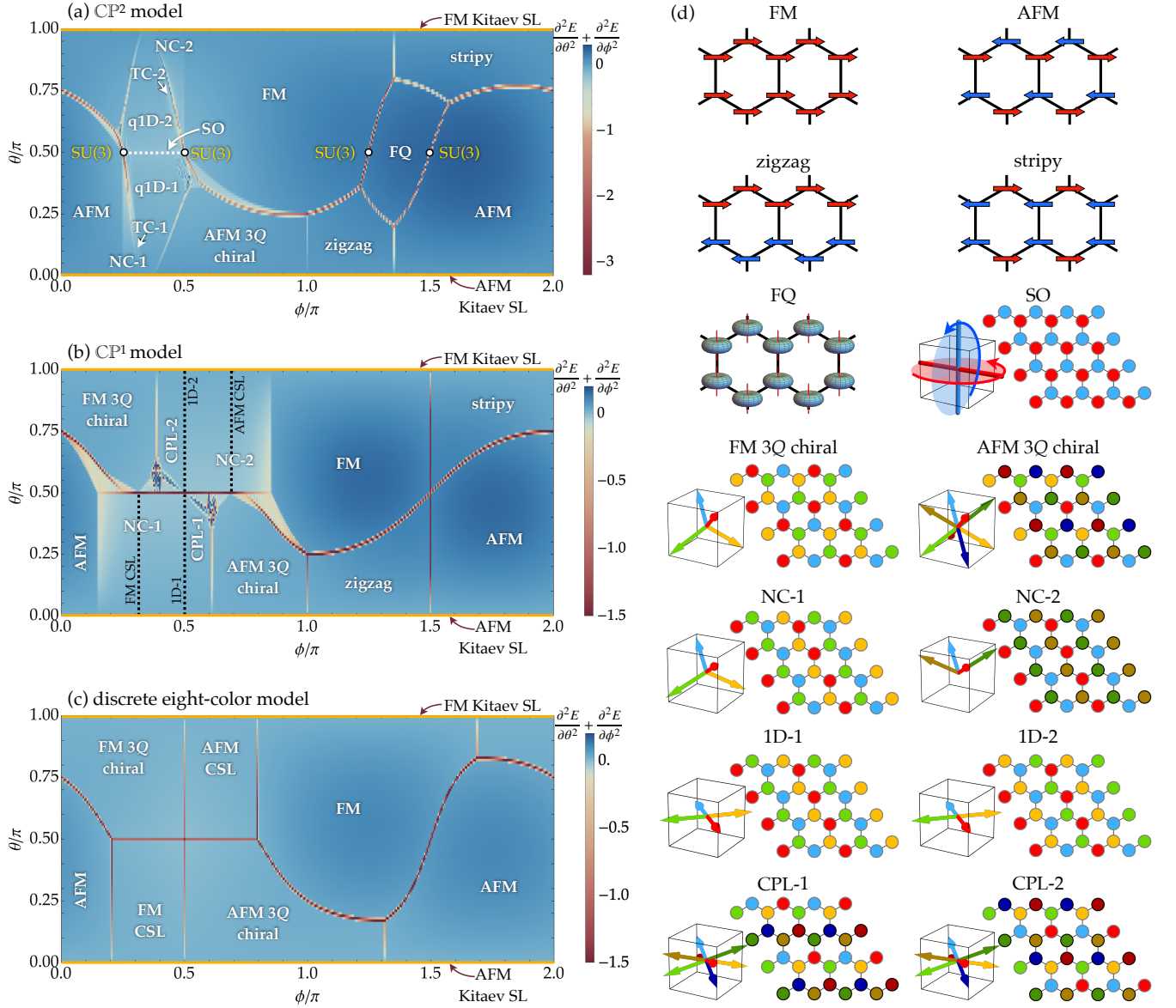


Figure 1. Ground-state phase diagrams in the 2D equirectangular projection as function of θ and ϕ [see Eq. (2)]. We plot the second derivative of the internal energy as contour color to make phase boundaries visible. (a) Solution of $\mathcal{H}_{\text{BBQ-K}}^A$ [see Eq. (7)] in the spin space \mathbb{CP}^2 , which accounts for all local degrees of freedom of an $S = 1$ moment, including dipolar and quadrupolar components. (b) Solution of $\mathcal{H}_{\text{BBQ-K}}^S$ [see Eq. (1)] in the spin space \mathbb{CP}^1 , which considers only dipolar degree of freedom of classical Heisenberg spins. (c) Solution of $\mathcal{H}_{\text{BBQ-K}}^{8c}$ for the discrete eight-color model [see Eq. (15)], where the dipolar degree of freedom is discretized and allowed to point only at the corners of a unit cube (see definition of spin states in Table I). (d) Real-space configurations of selected phases. Ferromagnetic (FM), antiferromagnetic (AFM), and triple- q chiral magnetic orders (FM 3Q chiral and AFM 3Q chiral), as well as the semiclassical analog of the Kitaev spin liquid (SL), are stabilized in all three phase diagrams. Noncoplanar (NC), (quasi-)one-dimensional (q1D / 1D), canted planar (CPL), and twisted conical (TC) phases are stabilized for the models with continuous degrees of freedom in (a) and (b), while ferroquadrupolar (FQ), and semiordered (SO) phases are purely quadrupolar in nature and are only stabilized in (a). FM and AFM chiral spin liquid (CSL) states emerge as the ground state along two singular lines in (b) and form a phase in (c). However, they do not appear in the ground state in (a), but instead become a stable phase at finite temperatures (see discussion in Sec. III D). Results in (a) and (b) were obtained by variational energy minimization for a finite-size cluster of $N_S = 28\,800$ spins under periodic boundary conditions, while (c) was solved analytically for the thermodynamic limit.

tanglement.

In this article, we expand on the theory discussed in our prior work, Ref. [75], with the goal of presenting a pedagogical explanation of the inherent nature of the CSL. To achieve this, we start by representing local $S = 1$ magnetic mo-

ments as $\text{SU}(3)$ spin-coherent states in the spin space \mathbb{CP}^2 . While this approach is semiclassical and does not include entanglement between spins, it properly accounts for the onsite quadrupole and dipole characteristics expected for $S = 1$ moments [47]. We proceed by systematically reducing the de-

degrees of freedom for local spins to the submanifold of $SU(2)$ spin-coherent states in the spin space \mathbb{CP}^1 . This representation treats spins as classical dipole vectors pointing to the Bloch sphere, as done in conventional Monte Carlo (MC) simulations for classical Heisenberg spins. Finally, we introduce a minimal model, the eight-color model, in which dipolar spins are restricted to eight discrete states, reminiscent of an eight-states clock model. The corresponding phase diagrams for each of these cases are depicted in Figs. 1(a), 1(b), and 1(c). The eight-color model, inspired by insights from simulations using the \mathbb{CP}^1 and \mathbb{CP}^2 models, effectively captures all physical properties of the CSL and enables us to understand its characteristics analytically. The simplicity of the eight-color model allows us to identify local bond constraints that unequivocally determine all observed properties of this CSL. It also allows us to implement a hexagon cluster update, which connects different states in the spin liquid manifold and dramatically reduces correlation times in numerical simulations. We complement our analysis with results for the dynamical structure factor, unveiling a gapped continuum of excitations.

The remainder of this article is structured as follows. In Sec. II, we introduce the $S = 1$ BBQ-Kitaev model on the honeycomb lattice. We analyze the same model for different local spin degrees of freedom, namely, $SU(3)$ spin-coherent states of \mathbb{CP}^2 (the \mathbb{CP}^2 model) which contain onsite dipole and quadrupole moments, $SU(2)$ spin-coherent states of \mathbb{CP}^1 (the \mathbb{CP}^1 model) which contain only onsite dipole moments, and the eight-color model which allows for only eight discretized dipolar spin states. In Sec. III, we present ground-state and finite-temperature results of the BBQ-Kitaev model. In Sec. III A, we discuss the influence of the local spin degree of freedom by explicitly comparing the ground-state phase diagrams between the \mathbb{CP}^2 , the \mathbb{CP}^1 , and the eight-color models. In Sec. III B, we discuss the eight-color model and provide an analytical explanation for all fundamental properties of the observed CSL, substantiated by comparisons to numerical simulations. In Sec. III C, we show numerical results for the \mathbb{CP}^1 model, and show that thermodynamic properties of the eight-color CSL remain intact even for continuous degrees of freedom. In Sec. III D, we show numerical results for the \mathbb{CP}^2 model, demonstrating that the CSL becomes an entropy-driven spin liquid at finite temperature. In Sec. III E, we present dynamical signatures of the CSL in the \mathbb{CP}^2 model, showing a largely gapped continuum of excitations. We conclude our work in Sec. IV with a brief summary and perspectives for possible future directions and experimental realizations.

II. BBQ-KITAEV MODEL WITH DIFFERENT SPIN DEGREES OF FREEDOM

We are interested in solving the bilinear-biquadratic (BBQ) model under influence of Kitaev interactions for $S = 1$ magnetic moments on the honeycomb lattice. The Hamiltonian is

given by

$$\mathcal{H}_{\text{BBQ-K}}^S = \sum_{\langle i,j \rangle} [J_1 \mathbf{S}_i \cdot \mathbf{S}_j + J_2 (\mathbf{S}_i \cdot \mathbf{S}_j)^2] + K \sum_{\alpha=x,y,z} \sum_{\langle ij \rangle_\alpha} S_i^\alpha S_j^\alpha, \quad (1)$$

where J_1 , J_2 , and K respectively account for the Heisenberg (bilinear), biquadratic, and Kitaev interaction strengths on nearest-neighbor bonds. The index $\alpha = x, y, z$ selects the spin- and bond-anisotropic Kitaev interactions on the honeycomb lattice [76]. We normalize the total interaction strength as

$$(J_1, J_2, K) = (\sin \theta \cos \phi, \sin \theta \sin \phi, \cos \theta), \quad (2)$$

and use the angles θ and ϕ as new model parameters. In this form, $\mathcal{H}_{\text{BBQ-K}}^S$ recovers the well-known limits of the BBQ model for $\theta/\pi = 0.5$ ($K = 0$), the AFM Kitaev model at $\theta/\pi = 0$ ($K = 1, J_1 = J_2 = 0$), the FM Kitaev model at $\theta/\pi = 1$ ($K = -1, J_1 = J_2 = 0$), and the Kitaev-Heisenberg model for $\phi/\pi = 0$ and 1 ($J_2 = 0$).

An $S = 1$ moment contains three magnetic states with $S^z = \{1, 0, -1\}$, which are mathematically described by the $\mathfrak{su}(3)$ algebra and contain magnetic dipole and quadrupole components. To correctly describe all fluctuations of such an $S = 1$ moment, we adopt the recently developed $U(3)$ formalism [47], an approach equivalent to the concept of $SU(3)$ spin-coherent states [22, 46, 48, 49, 77–79], and suitable to access not only thermodynamic properties, but also dynamical properties of $S = 1$ magnets at finite temperatures. By embedding the underlying $\mathfrak{su}(3)$ algebra into the larger $\mathfrak{u}(3)$ algebra with an additional spin-length constraint, this formalism becomes capable of simultaneously evaluating dipole and quadrupole fluctuations at each site, despite the drawback of losing quantum entanglement across the lattice.

In the $U(3)$ formalism, each localized $S = 1$ moment is represented by a 3×3 Hermitian matrix

$$\mathcal{A}_\beta^\alpha = (\mathbf{d}^\alpha)^* \mathbf{d}_\beta, \quad (3)$$

which we shall call henceforth the \mathcal{A} matrix. The \mathcal{A} matrix is formally a tensor, as defined in Ref. [47], where the superscript α and subscript β denote the row and column of each index, respectively. The \mathcal{A} matrices can be written in terms of complex vectors \mathbf{d}

$$\mathbf{d} = \begin{pmatrix} x_1 + i x_2 \\ x_3 + i x_4 \\ x_5 + i x_6 \end{pmatrix}, \quad (4)$$

also known as directors [23, 24]. We implicitly respect the spin-length constraint on the directors

$$\mathbf{d}^* \mathbf{d} = |\mathbf{d}|^2 = 1, \quad (5)$$

by parametrizing its components as

$$\begin{aligned}
 x_1 &= \theta_2^{1/4} \theta_1^{1/2} \sin \phi_1, \\
 x_2 &= \theta_2^{1/4} \theta_1^{1/2} \cos \phi_1, \\
 x_3 &= \theta_2^{1/4} (1 - \theta_1)^{1/2} \sin \phi_2, \\
 x_4 &= \theta_2^{1/4} (1 - \theta_1)^{1/2} \cos \phi_2, \\
 x_5 &= (1 - \theta_2^{1/2})^{1/2} \sin \phi_3, \\
 x_6 &= (1 - \theta_2^{1/2})^{1/2} \cos \phi_3,
 \end{aligned} \tag{6}$$

with $0 \leq \theta_1, \theta_2 \leq 1$ and $0 \leq \phi_1, \phi_2, \phi_3 < 2\pi$. To fix the unphysical gauge we choose to make the z component of \mathbf{d} purely real by setting $\phi_3 = \pi/2$, providing in total four degrees of freedom with a restrained order-parameter space, formally known as the complex projective plane \mathbb{CP}^2 . In this formalism, Eq. (1) can be rewritten in a bilinear form as

$$\begin{aligned}
 \mathcal{H}_{\text{BBQ-K}}^{\mathcal{A}} = & \sum_{\langle ij \rangle} \left[J_1 \mathcal{A}_{i\beta}^{\alpha} \mathcal{A}_{j\alpha}^{\beta} + (J_2 - J_1) \mathcal{A}_{i\beta}^{\alpha} \mathcal{A}_{j\beta}^{\alpha} + J_2 \mathcal{A}_{i\alpha}^{\alpha} \mathcal{A}_{j\beta}^{\beta} \right] \\
 & - K \sum_{\langle ij \rangle_{\alpha}} \epsilon_{\beta}^{\alpha\gamma} \epsilon_{\delta}^{\alpha\eta} \mathcal{A}_{i\gamma}^{\beta} \mathcal{A}_{j\eta}^{\delta},
 \end{aligned} \tag{7}$$

where $\epsilon_{\beta}^{\alpha\gamma}$ is the Levi-Civita symbol. Here and hereafter, we adopt the Einstein convention of summing over repeated indices. We shall refer to this form of the Hamiltonian in the following as “ \mathbb{CP}^2 model”. The matrix \mathcal{A}_i simultaneously incorporates the information of dipole and quadrupole moments at site i , which can be extracted respectively with

$$S_i^{\alpha} = -i\epsilon_{\beta}^{\alpha\gamma} \mathcal{A}_{i\gamma}^{\beta}, \tag{8}$$

$$Q_i^{\alpha\beta} = -\mathcal{A}_{i\beta}^{\alpha} - \mathcal{A}_{i\alpha}^{\beta} + \frac{2}{3}\delta^{\alpha\beta} \mathcal{A}_{i\gamma}^{\gamma}, \tag{9}$$

where $\delta^{\alpha\beta}$ is the Kronecker delta. Here, we express spin quadrupoles in their symmetric and traceless rank-2 tensor form.

To compute the averaged spin-dipole and spin-quadrupole norms we respectively use

$$|\mathbf{S}| = \frac{1}{N_S} \sum_i^{N_S} |\mathbf{S}_i|, \tag{10}$$

$$|\mathbf{Q}| = \frac{1}{N_S} \sum_i^{N_S} |\mathbf{Q}_i|, \tag{11}$$

where vector components are expressed as

$$\mathbf{S}_i = \begin{pmatrix} S_i^x \\ S_i^y \\ S_i^z \end{pmatrix}, \tag{12}$$

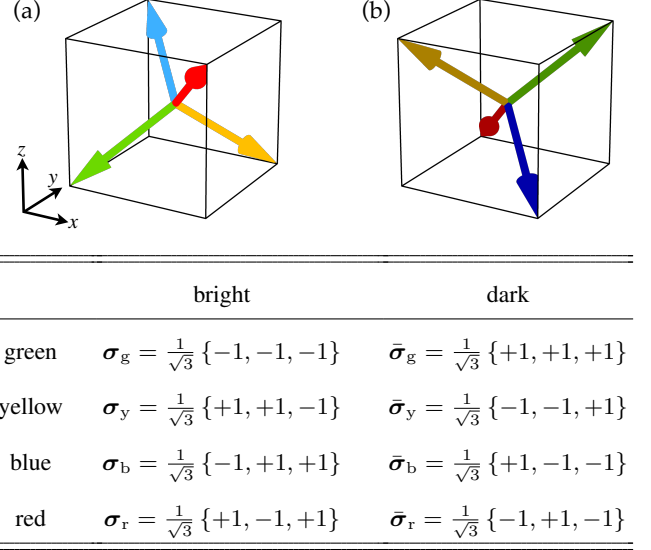


Table I. Definition of spin directions in the eight-color model of Eq. (15). For pedagogical reasons, we assign four colors to spins, namely “green”, “yellow”, “blue”, and “red”, and distinguish between their bright and dark contrast. Directions are explicitly shown in (a) for bright spins, and in (b) for dark spins.

and

$$\mathbf{Q}_i = \begin{pmatrix} Q_i^{x^2-y^2} \\ Q_i^{3z^2-r^2} \\ Q_i^{xy} \\ Q_i^{xz} \\ Q_i^{yz} \end{pmatrix} = \begin{pmatrix} \frac{1}{\sqrt{3}} (Q_i^{xx} - Q_i^{yy}) \\ \frac{1}{\sqrt{3}} (Q_i^{zz} - \frac{1}{2}(Q_i^{xx} + Q_i^{yy})) \\ Q_i^{xy} \\ Q_i^{xz} \\ Q_i^{yz} \end{pmatrix}. \tag{13}$$

In Sec. III A, we find many nontrivial phases for the \mathbb{CP}^2 case, especially when the interactions frustrate the model. To gain a better intuition of the underlying physics in such nontrivial phases, we investigate Eq. (1) also in the spin space \mathbb{CP}^1 , by effectively excluding all quadrupole fluctuations and allowing only for fluctuations of local dipole moments. This simplification corresponds to the treatment of classical Heisenberg spins, formally expressed as spin-coherent states of $\text{SU}(2)$, which are parametrized by a point on the Bloch sphere

$$\mathbf{S} = \begin{pmatrix} \sin \theta_1 \cos \phi_1 \\ \sin \theta_1 \sin \phi_1 \\ \cos \theta_1 \end{pmatrix}, \tag{14}$$

with $0 \leq \theta_1 \leq 1$ and $0 \leq \phi_1 < 2\pi$, the two local degrees of freedom for each spin on the lattice. In what follows, we refer to this model as “ \mathbb{CP}^1 model”.

In the \mathbb{CP}^2 model, a CSL phase is stabilized at finite temperatures (see Sec. III D), while in the \mathbb{CP}^1 model, the CSL phase appears along singular lines in the ground state (see Sec. III C). In the CSL phase, we observe that spins align along well-defined, discrete directions, pointing to the eight corners of a unit cube (see detailed discussion in Sec. III B).

This observation motivated us to further simplify Eq. (1) by discretizing spins to only point to these eight corners. We call this model the “eight-color model”, whose Hamiltonian is given by

$$\mathcal{H}_{\text{BBQ-K}}^{\text{8c}} = \sum_{\langle i,j \rangle} [J_1 \boldsymbol{\sigma}_i \cdot \boldsymbol{\sigma}_j + J_2 (\boldsymbol{\sigma}_i \cdot \boldsymbol{\sigma}_j)^2] + K \sum_{\alpha=x,y,z} \sum_{\langle ij \rangle_{\alpha}} \sigma_i^{\alpha} \sigma_j^{\alpha}. \quad (15)$$

As shown in Table I, we assign colors to the eight discrete, noncoplanar dipole spins $\boldsymbol{\sigma}$ such as “green”, “yellow”, “blue”, and “red”, and distinguish between “bright” spins, $\boldsymbol{\sigma}_g$, $\boldsymbol{\sigma}_y$, $\boldsymbol{\sigma}_b$, and $\boldsymbol{\sigma}_r$, and “dark” spins, $\bar{\boldsymbol{\sigma}}_g$, $\bar{\boldsymbol{\sigma}}_y$, $\bar{\boldsymbol{\sigma}}_b$, and $\bar{\boldsymbol{\sigma}}_r$. This simplified model is specifically designed to transparently understand the nature of the exotic chiral ordered and disordered phases.

III. RESULTS

In our previous work in Ref. [75], we studied the ground state and thermodynamic properties of $\mathcal{H}_{\text{BBQ-K}}^S$ in Eq. (1), and revealed the existence of a chiral spin liquid (CSL) at finite temperatures. In the present study, we build up an intuition for the microscopic origin and nature of this exotic CSL state by systematically restricting the local spin degree of freedom. We begin with the SU(3) representation of Eq. (1), the \mathbb{CP}^2 model, given by $\mathcal{H}_{\text{BBQ-K}}^A$ in Eq. (7), which captures all allowed components of an $S = 1$ spin, namely continuous dipolar and quadrupolar moments described in the spin space \mathbb{CP}^2 . Further, we solve the original model, $\mathcal{H}_{\text{BBQ-K}}^S$ in Eq. (1), in the spin space \mathbb{CP}^1 , which allows for dipole moments only [see Eq. (14)]. Finally, we consider the discrete eight-color model, given by $\mathcal{H}_{\text{BBQ-K}}^{\text{8c}}$ in Eq. (15), where dipolar spin moments are allowed to point only along eight discrete directions (see Table I). All three models include the same BBQ-Kitaev interactions, however for different degrees of freedom in spin space. While certain results have been previously presented in our earlier work [75], we will include some of them here to make the present paper self-contained.

A. Ground-state phase diagrams

In Figs. 1(a)–1(c) we respectively show the ground-state phase diagrams of $\mathcal{H}_{\text{BBQ-K}}^A$, $\mathcal{H}_{\text{BBQ-K}}^S$, and $\mathcal{H}_{\text{BBQ-K}}^{\text{8c}}$, solved in the spin space \mathbb{CP}^2 , \mathbb{CP}^1 , and for discrete eight-color spins. To obtain Figs. 1(a) and 1(b), we performed variational energy minimization, using the gradient descent method based on the machine learning library JAX [80, 81] for sufficiently large finite-size clusters of $N_S = 2L^2 = 28\,800$ spins (linear dimension $L = 120$) under periodic boundary conditions (see Appendix A for further details). Figure 1(c) was obtained in the thermodynamic limit from analytic comparison of local bond energies. We plot the phase diagrams in their 2D equirectangular projections parametrized by Eq. (2), and visualize phase boundaries by plotting $\partial^2 E / \partial \theta^2 + \partial^2 E / \partial \phi^2$,

the sum of the second-order derivatives of the internal energy E with respect to θ and ϕ . The corresponding real-space spin configurations of selected states are shown in Fig. 1(d) with dipole moments depicted as arrows, and quadrupole moments in form of “directors” with “doughnut-shaped” spin-probability distributions [23, 24]. It is worth noting that the phase diagrams for \mathbb{CP}^1 and eight-color models exhibit a self-duality around the high-symmetry points $(\phi/\pi, \theta/\pi) = (0.5, 0.5)$ and $(\phi/\pi, \theta/\pi) = (1.5, 0.5)$. In contrast, the phase diagram for \mathbb{CP}^2 lacks this self-dual symmetry, due to the presence of quadrupole moments.

1. Phase diagram for \mathbb{CP}^2 model

In Fig. 1(a) we show the ground-state phase diagram of $\mathcal{H}_{\text{BBQ-K}}^A$ in Eq. (7), by considering the full spin order-parameter space \mathbb{CP}^2 . When the biquadratic interaction is ferromagnetic, namely J_2 is negative ($1.0 < \phi/\pi < 2.0$), the model offers a combination of phases which have previously been reported on the $S = 1$ Kitaev-Heisenberg model [61, 72] and the BBQ model [82]. These comprise dipolar orders, in the form of ferromagnetic (FM), antiferromagnetic (AFM), zigzag, and stripy phases, together with a ferroquadrupolar (FQ) spin nematic phase.

In contrast, when J_2 is positive ($0.0 < \phi/\pi < 1.0$), the model provides a number of unconventional phases which emerge from the competition between frustrated interactions. Adjacent to the zigzag and stripy phases, we find noncoplanar chiral ordered phases, also known as “tetrahedral” and “cubic” states [83–85], in which spins point to the corners of a unit cube [see Fig. 1(d)]. These chiral configurations are represented by superpositions of three spiral states, and hence called triple- q states. The FM 3 Q chiral state is characterized by an extended eight-site magnetic unit cell, where four out of eight possible spin directions are selected and induce a net scalar spin chirality of $|\kappa|^{\text{FM chiral}} = 8/(3\sqrt{3})$ [see the definition of κ in Eq. (B8) of Appendix B]. The AFM 3 Q chiral state is essentially a reflection of the FM 3 Q chiral state, achieved by inverting spins on one of the two sublattices on the honeycomb lattice [see Fig. 1(d)], giving $|\kappa|^{\text{AFM chiral}} = 16/(3\sqrt{3})$. We note that the stripy and FM 3 Q chiral (zigzag and AFM 3 Q chiral) states are energetically degenerate at $\phi/\pi = 0$ ($\phi/\pi = 1$) along the vertical line for $0.75 \leq \theta/\pi < 1.0$ ($0.0 < \theta/\pi \leq 0.25$). However, this degeneracy is lifted by thermal fluctuations, which select the stripy (zigzag) phase, as confirmed by our MC simulations (not shown).

Between FM, AFM, and 3 Q chiral ordered phases, dipole and quadrupole moments mix in nontrivial ways, and produce a range of exotic states. In the limit of the BBQ model ($\theta/\pi = 0.5$), our semiclassical method realizes a semioordered (SO) (or semidisordered) [22, 86], purely quadrupolar state, connecting the two SU(3) points at $\phi/\pi = 0.25$ and $\phi/\pi = 0.5$ [87]. We note that this state is expected to be replaced by a plaquette valence bond crystal when quantum entanglement is fully taken into account [88]. Introducing nonzero Kitaev interactions ($\theta/\pi \neq 0.5$) immediately induces

the formation of a nonzero dipole moment $|\mathbf{S}| \neq 0$. To minimize the dominant BBQ interactions, dipolar components of the spins align orthogonal to their nearest neighbors within the xy , yz , or zx plane. In such a configuration, the Kitaev interaction energy is minimized on two bonds, while leaving the third one to be zero. Hence, dominant correlations prevail along zigzag chains and stabilize coplanar, quasi-one-dimensional (q1D) states in extended regions away from the BBQ limit. However, the presence of small quadrupolar correlations will induce a weak interchain coupling to form two-dimensional order.

Sandwiched between the q1D coplanar phases and the AFM/FM ordered phases, $\mathcal{H}_{\text{BBQ-K}}^A$ minimizes its energy by forming spin textures with noncoplanar (NC) orientation and incommensurate twisted conical (TC) states. These ordered states will give way to a finite-temperature chiral spin liquid (CSL) – not shown in Fig. 1(a) – which shall be the major focus of this study. We will discuss signatures of the CSL state explicitly for $\mathcal{H}_{\text{BBQ-K}}^A$ by including all allowed spin fluctuations of \mathbb{CP}^2 in Sec. III D, while building up an intuitive understanding of its microscopic origin by systematically restricting the allowed spin space to \mathbb{CP}^1 and further to discretized states in Secs. III C and III B, respectively.

2. Phase diagram for \mathbb{CP}^1 model

Many phases in Fig. 1(a) show dominant dipolar order mainly coming from the presence of bilinear Kitaev and Heisenberg interactions. To build up an intuitive understanding of the microscopic origin of these phases, and to quantitatively understand the influence of local quantum fluctuations in our model, we are going to restrict the order parameter space from \mathbb{CP}^2 to \mathbb{CP}^1 , by expressing an $S = 1$ moment by a classical Heisenberg vector, as parametrized with Eq. (14). In this way we only allow for purely dipolar spin states and exclude onsite quadrupole moments.

In this framework, by minimizing the energy of $\mathcal{H}_{\text{BBQ-K}}^S$ in Eq. (1), we obtain the ground-state phase diagram in Fig. 1(b). For negative J_2 ($1.0 < \phi/\pi < 2.0$) the model captures the same dominant dipolar FM, AFM, zigzag, and stripy ordered phases, as in the \mathbb{CP}^2 case. However, due to the exclusion of onsite quadrupolar degree of freedom, the FQ state is absent and has been replaced by a singular point at $\phi/\pi = 1.5$ and $\theta/\pi = 0.5$ where FM, AFM, zigzag, and stripy phases are energetically degenerate.

In the region where J_2 is positive ($0.0 < \phi/\pi < 1.0$), the model reproduces many phases as seen in Fig. 1(a), while the phase boundaries are rather strongly modified. We find noncoplanar FM and AFM $3Q$ chiral phases with same physical properties as in the \mathbb{CP}^2 case. Between AFM/FM ordered phases and AFM/FM $3Q$ chiral phases the model stabilizes NC phases and canted planar (CPL) phases with spin configurations shown in Fig. 1(d). Here, the NC phases are purely made of spin dipoles and exist in much wider regions compared to the \mathbb{CP}^2 case. At the phase boundary between the NC and CPL phases ($\phi/\pi = 0.5$), the model stabilizes coplanar, truly 1D phases, made of decoupled zigzag chains with

a subextensive ground-state manifold [see Fig. 1(d)]. While these 1D phases appear on a singular line in the \mathbb{CP}^1 model, the presence of quadrupole moments in the \mathbb{CP}^2 case stabilizes q1D phases (not truly 1D due to presence of small but nonzero quadrupolar order), in much wider regions of the phase diagram [see Fig. 1(a)].

Furthermore, the absence of quadrupole degrees of freedom allows the CSL state to exist in the ground state at the singular lines

$$\frac{\phi}{\pi} = \frac{1}{\pi} \arctan\left(\frac{3}{2}\right) \approx 0.312833, \quad 0.0 < \frac{\theta}{\pi} < 0.5, \quad (16)$$

for the FM CSL and at

$$\frac{\phi}{\pi} = 1 - \frac{1}{\pi} \arctan\left(\frac{3}{2}\right) \approx 0.687167, \quad 0.5 < \frac{\theta}{\pi} < 1.0, \quad (17)$$

for the AFM CSL, deep inside the NC phase. The analytic derivation of these values is described in Appendix C.

In the CSL ground state, spin-dipole moments point exactly to the eight discrete corners of the unit cube, similar to the ordered AFM/FM $3Q$ chiral states [see Fig. 1(d)]. However, in strong contrast to the chiral ordered states, the CSL does not break translational symmetries of the lattice, and hence exhibits an extensive degeneracy of states. This motivates us to further simplify the model by restricting the continuous spin space of \mathbb{CP}^1 to only eight discrete states (eight-color model), where dipolar spins are allowed to point only along the corners of a unit cube. We will explore this model in detail in the following subsections, and discuss ground-state and thermodynamic properties of the CSL explicitly for the \mathbb{CP}^1 model in Sec. III C.

3. Phase diagram for eight-color model

To understand the intriguing nature of this CSL, we analyze the eight-color model described by $\mathcal{H}_{\text{BBQ-K}}^{8c}$ in Eq. (15), which enables us to extract its most essential properties analytically. In this model we restrict the spin parameter space by allowing for only eight discrete dipolar spin directions, pointing along the corners of a unit cube, as defined in Table I.

As shown in the ground-state phase diagram in Fig. 1(c), this model stabilizes trivial magnetically-ordered states such as FM and AFM states in the region where the biquadratic interaction J_2 is mostly negative ($1.0 < \phi/\pi < 2.0$). For predominantly positive J_2 ($0.0 < \phi/\pi < 1.0$), the model stabilizes nontrivial chiral ordered, triple- q states, as also observed in the \mathbb{CP}^2 and \mathbb{CP}^1 models in Figs. 1(a) and 1(b), respectively. Since coplanar spin configurations are not allowed in this model, zigzag, stripy, 1D, and other states with canting angles away from the (111) axes are absent.

Importantly, between trivial magnetically-ordered and triple- q states, the model stabilizes the CSL states in wide regions of the phase diagram. The FM CSL phase exists for

$$\frac{1}{\pi} \arctan\left(\frac{3}{4}\right) < \frac{\phi}{\pi} < 0.5, \quad 0.0 < \frac{\theta}{\pi} < 0.5, \quad (18)$$

while the AFM CSL phase appears for

$$0.5 < \frac{\phi}{\pi} < 1 - \frac{1}{\pi} \arctan\left(\frac{3}{4}\right), \quad 0.5 < \frac{\theta}{\pi} < 1.0. \quad (19)$$

The phase boundaries can be obtained analytically by simple energy comparison, as described in Appendix C.

Both states are classical spin liquids with a nonzero scalar spin chirality and residual entropy at zero temperature, which is associated with their extensive number of degenerate ground states. We note that the phase boundary lines between chiral order and disordered phases at $\phi/\pi = 0.5$ and $\theta/\pi = 0.5$ also host classical spin liquids, which, however, has different properties than the CSL discussed here.

By comparison between measured physical observables, we argue that this CSL with all its properties survives in the \mathbb{CP}^1 and \mathbb{CP}^2 models, while additional degrees of freedom in spin space only weaken its stability in the phase diagram. For pedagogical reasons, we will start our journey by investigating the CSL on the eight-color model.

B. Analysis of eight-color model

In Fig. 1(c), we see that the eight-color model stabilizes the CSL ground state in wide regions of the phase diagram [see Eqs. (18) and (19)]. In Sec. III B 1, we use the simplicity of the eight-color model to analytically obtain bond-dependent spin constraints which determine the ground-state properties of this CSL. In Sec. III B 2, we validate our analytical results by numerical MC simulations and compare thermodynamic properties between the CSL and chiral ordered states.

1. Eight-color chiral spin liquid

The eight-color model given by $\mathcal{H}_{\text{BBQ-K}}^{8c}$ in Eq. (15) allows us to understand the nature of the CSL analytically from simple comparison of local bond energies. In the following, we consider the FM CSL for parameters outlined in Eq. (18), where all couplings are positive, with $0 < J_1 < 0.8$, $J_2 > 0.6$, and $K > 0$. Since $\mathcal{H}_{\text{BBQ-K}}^{8c}$ is symmetric in parameter space the following conclusions will also hold for the AFM CSL after inversion of the spin direction on one of the two sublattices on the honeycomb lattice.

We first compare energies in absence of Kitaev interactions at $\theta/\pi = 0.5$. The nearest-neighbor energy levels, exemplified for only “bright green” spins σ_g (see Table I), are given as

$$(\sigma_g, \sigma_g) : E = J_1 + J_2, \quad (20)$$

$$(\sigma_g, \bar{\sigma}_g) : E = -J_1 + J_2, \quad (21)$$

$$(\sigma_g, \bar{\sigma}_r), (\sigma_g, \bar{\sigma}_y), (\sigma_g, \bar{\sigma}_b) : E = \frac{1}{3}J_1 + \frac{1}{9}J_2, \quad (22)$$

$$(\sigma_g, \sigma_r), (\sigma_g, \sigma_y), (\sigma_g, \sigma_b) : E = -\frac{1}{3}J_1 + \frac{1}{9}J_2, \quad (23)$$

where the lowest-energy configurations in Eq. (23) exclude nearest neighbors of same color (e.g., “bright green”–“bright

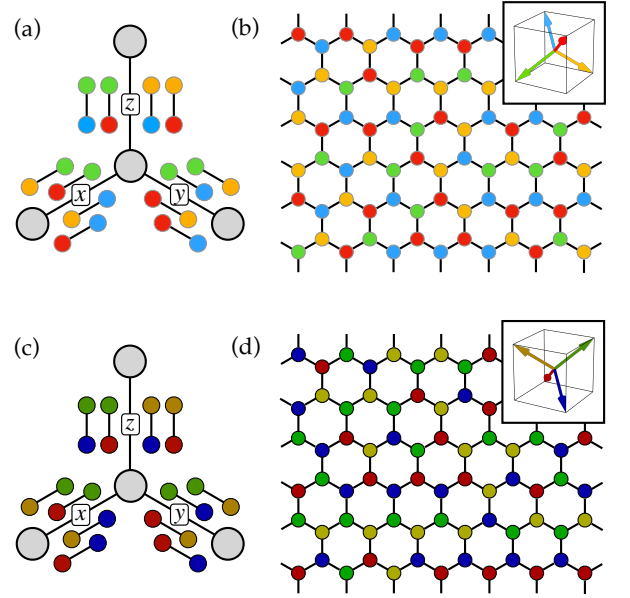


Figure 2. Macroscopic degeneracy in the FM chiral spin liquid (FM CSL). (a) Constraints on allowed color pairs on bonds for “bright” spins and (b) a corresponding representative spin configuration in the FM CSL ground-state manifold. Corresponding figures for “dark” spins are shown in (c) and (d). The definitions of spin orientations and colors are shown in the insets of (b) and (d) (see also Table I).

green”) and different contrast (e.g., “bright green”–“dark red”).

The degeneracy of the lowest-energy states can be lifted by introducing the bond-dependent Kitaev interactions, giving the ground state energy

$$E_{\text{GS}} = -\frac{1}{3}J_1 + \frac{1}{9}J_2 - \frac{1}{3}K. \quad (24)$$

Intriguingly, while $K < 0$ gives only one solution for Eq. (24) inducing FM $3Q$ chiral order, the case of $K > 0$ allows for multiple spin pairs (σ_g, σ_y) and (σ_g, σ_r) on the x bonds, (σ_g, σ_y) and (σ_g, σ_b) on the y bonds, and (σ_g, σ_b) and (σ_g, σ_r) on the z bonds. Since the Kitaev interactions couple spin components on each bond differently, the allowed color pairs in the ground state will be bond dependent.

By doing the same energy analysis for the other “bright” spins $(\sigma_y, \sigma_b, \sigma_r)$, we obtain the complete set of constraints on allowed color pairs on bonds:

$$(\sigma_g, \sigma_y), (\sigma_g, \sigma_r), (\sigma_b, \sigma_y), (\sigma_b, \sigma_r), \quad (25)$$

on the x bonds,

$$(\sigma_g, \sigma_y), (\sigma_g, \sigma_b), (\sigma_r, \sigma_y), (\sigma_r, \sigma_b), \quad (26)$$

on the y bonds, and

$$(\sigma_g, \sigma_b), (\sigma_g, \sigma_r), (\sigma_y, \sigma_b), (\sigma_y, \sigma_r), \quad (27)$$

on the z bonds. The same constraints apply for all “dark” colored spins. We visualize these bond constraints for “bright” and “dark” spins in Figs. 2(a) and 2(c), respectively.

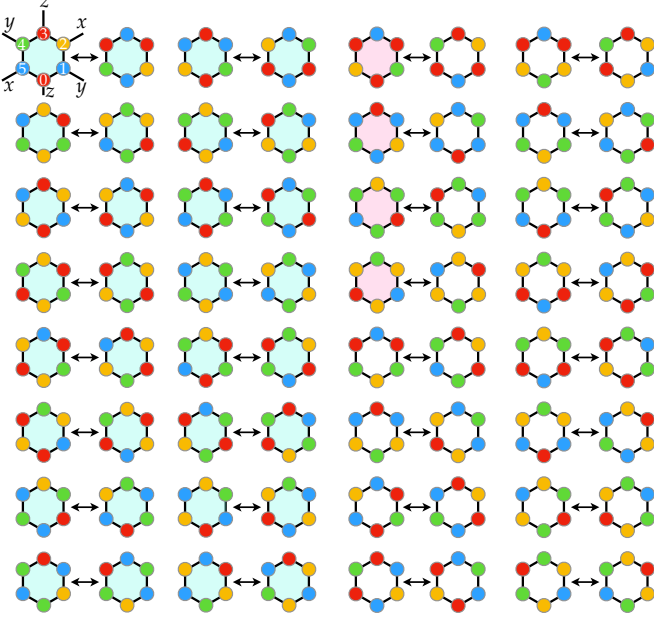


Figure 3. All allowed arrangements of “bright” spins on a single hexagon in the FM CSL state, with definitions for colors given in Table I. Configurations are arranged in pairs which are related to each other by a six-site hexagon cluster update following Eq. (28). Definitions of site indices and labels for the Kitaev bonds are shown on the top left hexagon. Hexagons are shaded in light cyan, pink, and white, indicating the value of scalar spin chirality $\kappa_p = -8/(3\sqrt{3})$, $16/(3\sqrt{3})$, and 0, respectively. All states exhibit $W_p = 1$ for the semiclassical analog of the \mathbb{Z}_2 -flux operator. Definitions of κ_p and W_p are given in Appendix B.

Every spin in the CSL ground state adheres to these bond constraints, as one can verify by examining Figs. 2(b) and 2(d), which depict representative spin configurations in the FM CSL ground-state manifold within “bright” and “dark” spin sectors, respectively. However, since every spin can choose between two different colored spins as their neighbors, the bond constraints are not strong enough to enforce long-range order.

The resulting extensive ground state manifold induces a nonzero residual entropy in the CSL, which can be understood from the fact that two spin configurations at one hexagon can always be transformed into each other by a local hexagon cluster update:

$$\mathbf{S}_{p,j}^{\text{new}} = R_j^\alpha \mathbf{S}_{p,j}, \quad (28)$$

where R_j^α is the rotation matrix of angle π about the axis $\alpha = x, y, z$; α is the site-dependent label for the Kitaev bond pointing outwards the hexagon p at site $j = 0, \dots, 5$ (see definition on site labels and α at top left in Fig. 3). In Fig. 3 we show all allowed spin configurations on a single hexagon in the “bright” manifold of the FM CSL, which are related by such a six-site hexagon update. Since the CSL allows always for two spin configurations per hexagon, we obtain the

normalized residual entropy in the ground state

$$\frac{S(T \rightarrow 0)}{N_S} = \frac{1}{N_S} \log 2^{N_h} = \frac{1}{2} \log 2, \quad (29)$$

where $N_h = N_S/2$ is the number of hexagons on the whole lattice. This is $1/6$ of the total entropy per site, $\log 8$.

Interestingly, the set of all possible states on a hexagon in Fig. 3 homogeneously exhibits a nonzero value for the octupole moment, $\sum_i S_i^x S_i^y S_i^z$, which induces broken time-reversal symmetry. This time-reversal symmetry breaking consequently generates a nonzero scalar spin chirality on each hexagon, κ_p , as we defined in Eq. (B9) of Appendix B. The 64 states per hexagon form three groups with different values of $\kappa_p = -8/(3\sqrt{3})$ (cyan), $16/(3\sqrt{3})$ (pink), and 0 (white) for 32, 4, and 28 states respectively, which results in the averaged nonzero value of

$$\begin{aligned} \kappa &= \frac{1}{64} \sum_p \kappa_p \\ &= \frac{1}{64} \left(-\frac{8}{3\sqrt{3}} \times 32 + \frac{16}{3\sqrt{3}} \times 4 + 0 \times 28 \right) \\ &= -\frac{1}{\sqrt{3}} \approx -0.577. \end{aligned} \quad (30)$$

Furthermore, we find that the semiclassical analog of the \mathbb{Z}_2 -flux operator, W_p , defined in Eq. (B14), gives $W_p = 1$ for every spin configuration in Fig. 3. We note that $W_p = -1$ for the AFM CSL, offering a way to distinguish the two spin liquids from each other.

Besides the residual entropy and nonzero scalar spin chirality, the bond-dependent spin constraints in the CSL ground state show extremely short-ranged spin correlations. As visualized in Fig. 2, nearest-neighbor color pairs are always of same contrast (“bright”–“bright” or “dark”–“dark”), but never of the same color. By comparison of spin components, as given in Table I, the correlations for all allowed nearest neighbors (distance $\ell = 1$) in the ground-state are therefore always exactly

$$D(\ell = 1) = \boldsymbol{\sigma}_i \cdot \boldsymbol{\sigma}_j = -\frac{1}{3}. \quad (31)$$

Yet again, by considering the same color constraints, one finds that spin configurations for next-nearest neighbors and beyond are all equally allowed and give on average

$$D(\ell > 1) = \boldsymbol{\sigma}_i \cdot \boldsymbol{\sigma}_k = 3 \times \left(-\frac{1}{3} \right) + 1 \times 1 = 0, \quad (32)$$

where the contribution 1×1 comes from a pair of the same color, which is forbidden for nearest neighbors, but allowed for further neighbors. Interestingly, such extremely short-range correlations coincide with analytical predictions for the $S = 1$ Kitaev SL in Ref. [57].

2. Finite-temperature properties of eight-color model

In Fig. 4 we show finite-temperature results from classical MC simulations of $\mathcal{H}_{\text{BBQ-K}}^{\text{bc}}$ in Eq. (15), for chiral ordered

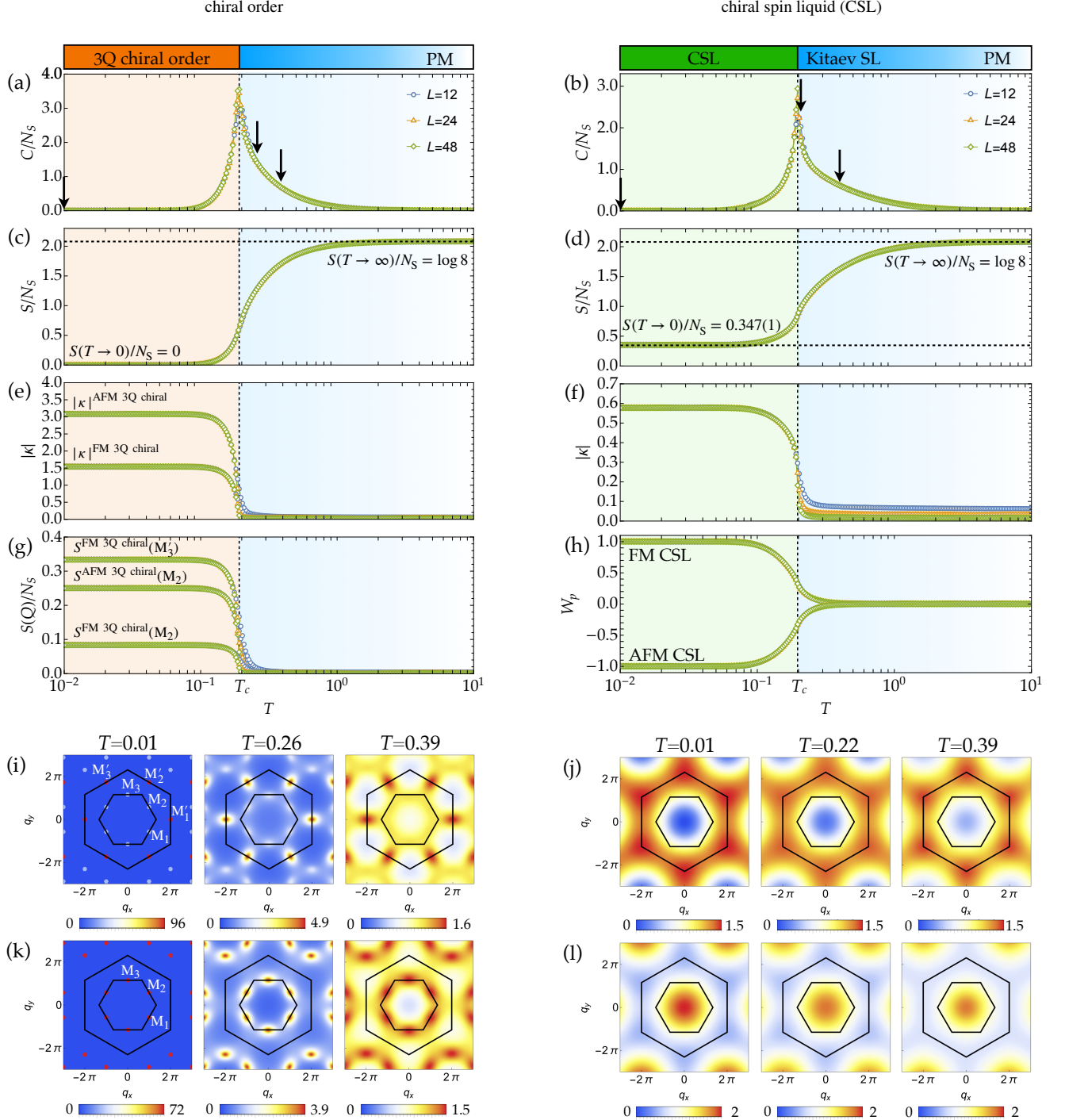


Figure 4. Comparison of thermodynamic quantities between the FM 3Q chiral ($\phi/\pi = 0.2$, $\theta/\pi = 0.9$) and AFM 3Q chiral ($\phi/\pi = 0.8$, $\theta/\pi = 0.1$) ordered phases (left column), and the FM CSL ($\phi/\pi = 0.35$, $\theta/\pi = 0.25$) and AFM CSL ($\phi/\pi = 0.65$, $\theta/\pi = 0.75$) phases (right column) for the eight-color model given by $\mathcal{H}_{\text{BBQ-K}}^{\text{8c}}$ in Eq. (15) [see the phase diagram in Fig. 1(c)]. Shown are the temperature dependencies of (a)–(b) the specific heat per site, C/N_S [Eq. (B1)], (c)–(d) the entropy per site, S/N_S [Eq. (B2)], and (e)–(f) the absolute value of the scalar spin chirality, $|\kappa|$ [Eq. (B8)]. (g) shows the spin structure factor $S_S(\mathbf{Q})$ [Eqs. (B3) and (B7)] for the chiral ordered phases at characteristic ordering vectors indicated in (i) and (k). (h) shows the semiclassical analog of the \mathbb{Z}_2 -flux operator [Eq. (B14)] for the CSL phases. The momentum resolved spin structure factors, $S_S(\mathbf{q})$, are shown for (i) the FM 3Q chiral ordered phase, (j) the FM CSL phase, (k) the AFM 3Q chiral ordered phase, and (l) the AFM CSL phase, for three different temperatures indicated by black arrows in (a) and (b). Data were obtained from classical MC simulations on clusters of size $L = 12, 24$, and 48 ($N_S = 288, 1152$, and 4608). $S_S(\mathbf{q})$ are shown for $L = 48$, except for (i) and (k) at $T = 0.01$, where $L = 12$.

phases (FM 3Q chiral at $\phi/\pi = 0.2$ and $\theta/\pi = 0.9$, and AFM 3Q chiral at $\phi/\pi = 0.8$ and $\theta/\pi = 0.1$), in the left column, and chiral liquid phases (FM CSL at $\phi/\pi = 0.35$ and $\theta/\pi = 0.25$, and AFM CSL at $\phi/\pi = 0.65$ and $\theta/\pi = 0.75$) in the right column for finite-size systems of linear dimension $L = 12, 24$, and 48 . Since the Hamiltonian is symmetric in parameter space, the FM and AFM states are related to each other by inversion of the spins on one sublattice of the honeycomb lattice. Therefore, energy related observables, such as the specific heat C [Eq. (B1)] and the entropy S [Eq. (B2)] are identical for the FM and AFM states (here shown only once), while magnetic observables, like the scalar spin chirality κ [Eq. (B8)], the spin structure factor $S_S(\mathbf{q})$ [Eqs. (B3) and (B7)], and the semiclassical analog of the W_p flux operator [Eq. (B14)] are distinct.

The specific heat, C [Eq. (B1)], in the first row of Fig. 4, exhibits a sharp singularity at (a) $T_c = 0.186(5)$ and (b) $T_c = 0.192(5)$ [89]. At these transition temperatures, the system spontaneously breaks its chirality by selecting a configuration where spins are either all bright or all dark in the FM 3Q chiral ordered and FM CSL states [see Eq. (23) and discussion in Sec. III B 1]. Due to the symmetry of the Hamiltonian in parameter space, the AFM counterparts of these states similarly break chirality. However, in the AFM versions, there is a mixture of bright and dark spins due to the inversion of spins on one sublattice of the honeycomb lattice. We confirmed the transition into the CSL to be a second-order phase transition, following the \mathbb{Z}_2 Ising universality class. The selection of either bright or dark spins generates a nonzero octupolar moment, $\sum_i S_i^x S_i^y S_i^z$, which acts as an Ising order parameter. This parameter is time-reversal odd, and consequently leads to the development of a nonzero scalar spin chirality. We leave more detailed analyses for future work.

Even though, the spontaneous breaking of chirality seems identical, the left column of Fig. 4 shows a transition into a magnetically ordered state, while the right column corresponds to a transition into the disordered CSL state. This can be directly confirmed in the second row of Fig. 4, which shows the entropy, S [see Eq. (B2)], as obtained from numerical integration of the specific heat over the available temperature range $10^{-2} \leq T \leq 10$. The total entropy of the system, $\log 8$, is released by passing through the phase transition at T_c , resulting in zero entropy $S(T \rightarrow 0)/N_S = 0$ in the chiral ordered states as shown in Fig. 4(c). In contrast, the CSLs in Fig. 4(d) show a residual entropy of

$$\frac{S(T \rightarrow 0)}{N_S} = 0.347(1) \approx \frac{1}{2} \log 2, \quad (33)$$

which matches with the analytically predicted value in Eq. (29), and is direct numerical evidence of a disordered ground state with extensive degeneracy.

Furthermore, in Figs. 4(e) and 4(f) we show the absolute value of the scalar spin chirality, $|\kappa|$ [see Eq. (B8)], for the ordered and disordered chiral states. In both cases, $|\kappa|$ scales to zero above T_c , and becomes nonzero below T_c . At low temperatures, we measure for the FM and AFM 3Q chiral ordered

states the following values

$$|\kappa|^{\text{FM 3Q chiral}} = 1.5396(1) \approx \frac{8}{3\sqrt{3}}, \quad (34)$$

$$|\kappa|^{\text{AFM 3Q chiral}} = 3.0792(1) \approx \frac{16}{3\sqrt{3}}, \quad (35)$$

and for the FM and AFM CSL states commonly

$$|\kappa|^{\text{CSL}} = 0.5774(1) \approx \frac{1}{\sqrt{3}}. \quad (36)$$

Yet again, the result for the CSL matches very well with our analytical estimate in Eq. (30). Furthermore, as shown in Fig. 4(h), the semiclassical analog of the \mathbb{Z}_2 -flux operator reaches perfectly $W_p = 1$ in the FM CSL, and $W_p = -1$ in the AFM CSL, as expected analytically.

Characteristic magnetic signatures, which clearly distinguish ordered from disordered states, can be found in the dipolar equal-time structure factor $S_S(\mathbf{q})$ [see Eqs. (B3) and (B7)]. We show the $S_S(\mathbf{q})$ at three different temperatures indicated by black arrows in Fig. 4(a), for the FM and AFM 3Q chiral ordered phases in Figs. 4(i) and 4(k), respectively. By reducing the temperature, the spectral weight accumulates around the M points in the Brillouin zone. Below T_c , Bragg peaks develop at the M_1 , M_2 , and M_3 points in the AFM 3Q chiral state. Additionally, Bragg peaks appear at the M'_1 , M'_2 , and M'_3 points in the FM 3Q chiral state. These clearly identify both phases as triple- q ordered states. The intensities of selected Bragg peaks are explicitly shown as functions of temperature in Fig. 4(g).

Meanwhile, the $S_S(\mathbf{q})$ for the CSL phases behave very differently. In Figs. 4(j) and 4(l) we show the $S_S(\mathbf{q})$ for the FM and AFM CSL states, respectively, at three different temperatures indicated by black arrows in Fig. 4(b). The signal is very diffuse and does not show any qualitative difference below and above T_c . In fact, the scattering function is reminiscent of the $S_S(\mathbf{q})$ for the Kitaev SL [90], showing very diffuse scattering around the Brillouin zone edge in the FM CSL, and accumulation of intensity around the Γ point in the AFM CSL. This diffuse scattering signature and the absence of any Bragg peaks are the direct evidence of a magnetically disordered state below T_c .

Since momentum-resolved spin-spin correlations of the CSL seem very similar to those in the Kitaev SL, we investigate correlations also in real space. Figure 5 shows the MC data of the spin-spin correlations

$$D(\ell) = \langle \sigma_0 \cdot \sigma_\ell \rangle, \quad (37)$$

in the FM CSL at $\phi/\pi = 0.35$ and $\theta/\pi = 0.25$ measured at five different temperatures. The correlations are averaged over symmetrically equivalent paths and are plotted semilogarithmically, where ℓ corresponds to the Manhattan distance along zigzag chains on the honeycomb lattice. For temperatures above T_c , correlations decay exponentially, with increasing correlation length upon reduction of T . Below T_c , the behavior changes dramatically and exhibits strong nearest-neighbor correlations with $|D(\ell = 1)| = 0.3333(1)$ at the

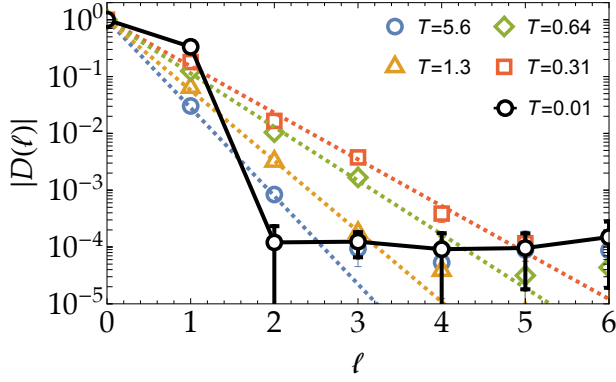


Figure 5. Semilogarithmic plot of spin-spin correlations $|D(\ell)|$ [see Eq. (37)] for the FM CSL case at five different temperatures. Correlations show an exponential decay above the critical temperature $T_c = 0.192(5)$ [peak in Fig. 4(b)]. Below T_c , correlations show a large value for nearest-neighbor contributions, $|D(\ell=1)| = 0.3333(1)$, and a negligibly small value beyond nearest neighbors, $|D(\ell > 1)| \lesssim 10^{-4}$. Data were obtained from classical MC simulations of the eight-color model given by $\mathcal{H}_{\text{BBQ-K}}^{\text{8c}}$ in Eq. (15), at model parameters $\phi/\pi = 0.35$ and $\theta/\pi = 0.25$, for a cluster of size $L = 48$ ($N_S = 4608$). Correlations are shown as function of the Manhattan distance ℓ , and were obtained after averaging over symmetrically equivalent paths along zigzag chains on the honeycomb lattice.

lowest measured temperatures $T = 0.01$, while correlations beyond the nearest neighbors become negligibly small with $|D(\ell > 1)| \lesssim 10^{-4}$. These results confirm our analytical prediction in Eqs. (31) and (32) of extremely short-range correlations in the CSL.

In short summary of this subsection, our investigation focused on a simplified model, the eight-color model, $\mathcal{H}_{\text{BBQ-K}}^{\text{8c}}$ in Eq. (15), with the aim of unraveling the unique nature and nontrivial characteristics of the eight-color CSL. We discovered that the CSL is characterized by bond-dependent spin constraints, as visualized in Fig. 2, giving rise to exotic properties such as residual entropy, nonzero scalar spin chirality, nonzero \mathbb{Z}_2 -flux order parameter, and extremely short-range spin correlations. We have successfully verified the existence of all these properties through unbiased numerical MC simulations.

C. Analysis of \mathbb{CP}^1 model

In the previous section, we investigated the eight-color model, as a simplification of the original BBQ-Kitaev model, $\mathcal{H}_{\text{BBQ-K}}^S$ in Eq. (1), by discretising the continuous spin space of an $S = 1$ moment to only eight allowed, noncoplanar states. This helped us to transparently understand the nature and origin of the exotic CSL phase in a simple analytical way.

In this section, we are going to partially relax this constraint, and allow dipolar spin components to take continuous values, namely being a classical Heisenberg vector described in the order parameter space \mathbb{CP}^1 . Compared to the eight-

color model, the \mathbb{CP}^1 model, with its enlarged spin space, offers a variety of additional and nontrivial phases. Understanding these phases will help us in bridging our comprehension from the simplified eight-color model to the more complex \mathbb{CP}^2 model.

1. Ground-state properties of \mathbb{CP}^1 model

In Fig. 6(a) we show a zoom-in of the ground-state phase diagram in Fig. 1(b) for positive J_2 ($0.0 < \phi/\pi < 1.0$), where the model is mostly frustrated. Between FM/AFM ordered and FM/AFM 3Q chiral phases the model stabilizes NC phases, and canted planar (CPL) phases over a wide range of model parameters. The canting angle of spins in those phases depends on the model parameters. Notably, specific choices of ϕ allow us to stabilize disordered CSLs and dimensionally-reduced 1D phases in the ground state, as indicated by the black dotted lines in Fig. 6(a) [91].

To see these phase competitions in more detail, in Fig. 6(b) we concentrate on the lower part of the phase diagram at $\theta/\pi = 0.06$ [red line in Fig. 6(a)], and explicitly show the normalized energy, E/N_S , and its derivative, $\partial(E/N_S)/\partial\phi$ (top), together with the $S_S(\mathbf{q})$ [Eqs. (B3) and (B7)] at relevant ordering vectors \mathbf{K}' , \mathbf{M}_1 , \mathbf{M}_2 , \mathbf{M}_3 , and \mathbf{M}'_3 (bottom). The transition from CPL-1 to AFM 3Q chiral phase at $\phi/\pi \approx 0.611$ is of first order (solid black line), while transitions from AFM to NC-1 at $\phi/\pi \approx 0.148$ and NC-1 to CPL-1 at $\phi/\pi = 0.5$ are of second order (dashed black lines), as seen by a jump and kinks in $\partial(E/N_S)/\partial\phi$, respectively. The Bragg peaks at the \mathbf{K}' points monotonically reduce their intensity in the NC-1 phase as ϕ increases, while additional ordering vectors at the \mathbf{M}_2 and \mathbf{M}'_3 points increase. In the CPL-1 phase, intensities at the \mathbf{M}_3 and \mathbf{M}_1 points become also nonzero, while the AFM 3Q chiral state shows an equal weight at the \mathbf{M}_1 , \mathbf{M}_2 , and \mathbf{M}_3 points, forming the triple- q order, as also obtained in the eight-color model in Fig. 4(k).

In Fig. 6(c) we show the energy difference $\Delta E/N_S$ between the FM CSL (yellow circles) and the 1D-1 state (blue circles) relative to the ground state for $\theta/\pi = 0.06$. The lower insets illustrate the spin configurations within each ordered phase, while the upper insets represent metastable states of the FM CSL. Upon increasing ϕ/π above ≈ 0.148 , spins in the ground state start to cant away from the collinear AFM arrangement to establish the NC-1 order, with a four-site magnetic unit cell [see Fig. 1(d)]. The canting angle of spins in the NC-1 phase is ϕ dependent, and the spontaneous selection of a particular direction for this canting angle induces a single- q order with Bragg peaks at the \mathbf{M}_2 points in the first Brillouin zone, supplemented by other peaks in the extended Brillouin zone [see Fig. 6(b)].

Upon tuning the model to $\phi/\pi = (1/\pi) \arctan(3/2)$ [see Eq. (16)], the spins achieve isotropic alignment across the lattice, by pointing precisely towards the corners of a unit cube. At this critical point, the system allows an extensive number of spin configurations to form the CSL ground state, characterized by all properties as discussed on the eight-color model in Sec. III B 1. In the vicinity of this critical point, we find a CSL

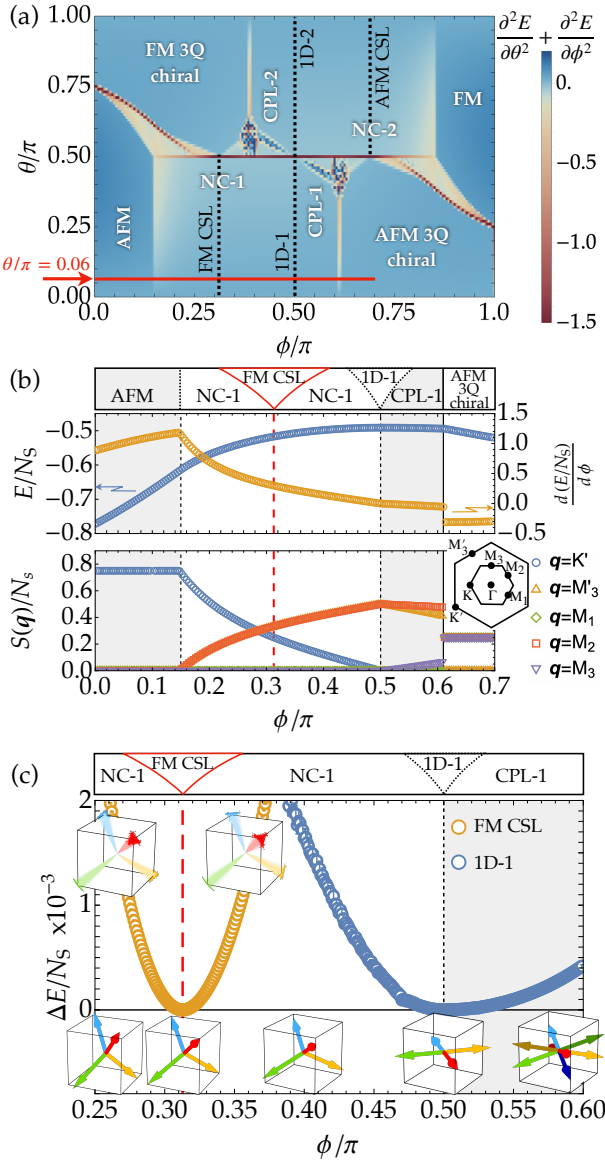


Figure 6. Competing phases of $\mathcal{H}_{\text{BBQ-K}}^S$ in Eq. (1) for classical Heisenberg spins (\mathbb{CP}^1 model), obtained by variational energy minimization for a finite-size cluster of linear dimension $L = 120$ ($N_S = 28\,800$ spins) under periodic boundary conditions. (a) Zoom-in of the ground-state phase diagram in Fig. 1(b) to the region for $0.0 \leq \phi/\pi \leq 1.0$. (b) Normalized energy and its derivative, E/N_S and $\partial(E/N_S)/\partial\phi$, (top), and the structure factor for dipole moments, $S_S(\mathbf{q})$ [Eqs. (B3) and (B7)], at high-symmetry momenta (bottom) at $\theta/\pi = 0.06$ [red line in (a)]. The solid and dashed lines represent first- and second-order phase transitions, respectively. (c) Energy difference, $\Delta E/N_S$, measured from the ground state to the metastable FM CSL and 1D-1 phases at $\theta/\pi = 0.06$. The lower insets show spin configurations in each ordered phase, while the upper ones represent metastable states of the FM CSL.

like state as a metastable state. Spins in this metastable CSL are slightly canted away from the (111) directions as shown in the insets of Fig. 6(c), while still retaining the underlying nature of the CSL with macroscopic degeneracy.

Upon further increasing ϕ , spins in the NC-1 ground state continue to cant until they achieve complete coplanarity, precisely at the boundary between the NC-1 and CPL-1 phases, at $\phi/\pi = 0.5$. At this specific point, nearest-neighbor spins are mutually orthogonal to each other, and effectively cancel nearest-neighbor bilinear and biquadratic interactions. Coplanar spins globally select either the xy , yz , or zx plane [the inset of Fig. 6(c) shows the case of the xy plane], by setting one of their spin components to zero. Therefore the dominating Kitaev interactions for one particular bond-type will be zero, and effectively decouple individual zigzag chains throughout the whole lattice. The system effectively forms a dimensionally-reduced 1D phase. Increasing ϕ beyond this point will again impose canting of spins, but this time with an enlarged eight-site magnetic unit cell forming the magnetic order of the CPL-1 state [see Fig. 1(d)].

2. Finite-temperature properties of \mathbb{CP}^1 model

Let us now turn to the thermodynamic properties of the CSL in the \mathbb{CP}^1 model. In Fig. 7, we show results from classical MC simulations of $\mathcal{H}_{\text{BBQ-K}}^S$ in Eq. (1), at model parameters $\theta/\pi = 0.06$ and $\phi/\pi = (1/\pi) \arctan(3/2)$, which stabilize the FM CSL in the ground state [see Eq. (16)].

In Figs. 7(a)–7(c) we respectively show the specific heat C/N_S [Eq. (B1)], the scalar spin chirality $|\kappa|$ [Eq. (B8)], and the semiclassical analog of the \mathbb{Z}_2 -flux operator, W_p [Eq. (B14)], over a wide range of temperatures. C/N_S shows a clear singularity at $T_c = 0.0193(6)$, which scales weakly with system size, and has a shape which looks somewhat similar to the observed singularity in the eight-color model in Fig. 4(b).

For $T \rightarrow 0$, we observe $C/N_S \rightarrow 1$, as expected for classical Heisenberg spins in the absence of soft mode excitations. We note that the acceptance ratio for single-spin flip updates at such low temperatures becomes strongly suppressed (see Appendix D), suggesting that continuous local spin motion is not able to adiabatically connect different ground-state configurations. However, where the single-spin flip fails, the hexagon update becomes successful, demonstrating that in the CSL phase decorrelation primarily occurs through cluster updates [see Eq. (28)].

The scalar spin chirality $|\kappa|$ scales to zero in the paramagnetic regime, and takes nonzero values below T_c , as observed in the eight-color model in Fig. 4(f). However, in comparison, $|\kappa|$ does not rapidly saturate, but rather monotonically reaches a value slightly smaller than in the eight-color model [see Eq. (36)]. We note that the asymptotic value of $|\kappa|$ becomes θ dependent (not shown here). However, variational energy minimization confirms that at $T = 0$, spins precisely align along the (111) direction, as also illustrated in the lower insets of Fig. 6(c). This seemingly contradictory observation implies that different configurations of the CSL ground state manifold in Fig. 3 are selected with varying weights in the \mathbb{CP}^1 model, resulting in a reduction of κ at finite T . At the lowest temperatures, the \mathbb{Z}_2 -flux operator takes a value $W_p \approx 1$, as observed in the eight-color model.

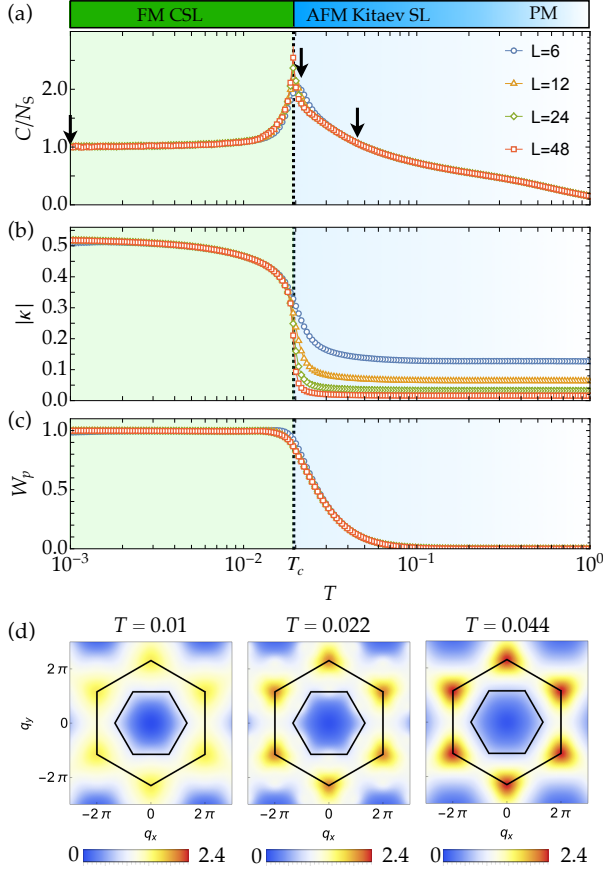


Figure 7. Finite-temperature properties of the FM CSL phase for the \mathbb{CP}^1 model given by $\mathcal{H}_{\text{BBQ-K}}^S$ in Eq. (1) at $\phi/\pi = (1/\pi) \arctan(3/2)$ and $\theta/\pi = 0.06$. Shown are temperature dependencies of (a) the specific heat per site, C/N_S [Eq. (B1)], (b) the absolute value of the scalar spin chirality $|\kappa|$ [Eq. (B8)], and (c) the semiclassical analog of the \mathbb{Z}_2 -flux operator, W_p [Eq. (B14)]. MC simulations were performed for $L = 6, 12, 24$, and 48 ($N_S = 72, 288, 1152$, and 4608). (d) shows the spin structure factor $S_S(\mathbf{q})$ [Eqs. (B3) and (B7)] at temperatures indicated by black arrows in (a) for $L = 24$.

In Fig. 7(d) we show the spin structure factor $S_S(\mathbf{q})$ at three different temperatures indicated by black arrows in Fig. 7(a). The signal is diffuse across the entire range of temperatures and closely resembles the spin structure factor of the eight-color FM CSL [see Fig. 4(j)] with an enlarged concentration of intensity around the K' points [see inset in Fig. 6(b)] and, almost invisible, some additional weak intensity accumulation around the M points in the first Brillouin zone at $T = 0.022$.

Thermodynamic properties for the CSL in both the eight-color model and the \mathbb{CP}^1 model match remarkably well. This alignment provides strong evidence that the eight-color CSL, with all of its physical properties analyzed in Sec. III B 1, remains preserved even after relaxing the spin degree of freedom to \mathbb{CP}^1 . Given that the CSL persists as a metastable state in the vicinity of its optimal model parameters given by Eq. (16) [see Fig. 6(c)], we anticipate its survival for an enlarged region of model parameters at finite temperatures due

to the substantial entropy associated with its macroscopic degeneracy.

D. Analysis of \mathbb{CP}^2 model

The original BBQ-Kitaev model allows for both dipole and quadrupole components of $S = 1$ magnetic moments, which are correctly described in the spin space \mathbb{CP}^2 . In the last two subsections we simplified this model by restricting the spin degree of freedom to extract the essential properties of the CSL state. In the present subsection we come back to the original model by reintroducing all allowed degrees of freedom for $S = 1$ moments. We will not only see that the CSL survives at finite temperatures even in the presence of quadrupolar degree of freedom, but also quantitatively examine the impact of local quantum fluctuations on the ground-state phase diagram. Some results in this subsection have already been presented in our earlier work in Ref. [75], but we include them here to make the discussion and comparison to \mathbb{CP}^1 and eight-color models self-contained.

1. Ground-state properties of \mathbb{CP}^2 model

In Fig. 8(a), we show the spin-dipole norm, $|\mathbf{S}|$ [see Eq. (10)], in the frustrated region of the phase diagram in Fig. 1(a). In most of the phases, the spin norm is $|\mathbf{S}| \neq 1$, indicating the presence of nonzero onsite quadrupole moments. The onsite dipole and quadrupole moments mix in nontrivial ways to alleviate frustration, leading to quantitative changes in phases and their boundaries, in contrast to the \mathbb{CP}^1 model shown in Fig. 6(a).

The purely quadrupolar SO phase at $\theta/\pi = 0.5$ [see Fig. 1(d)], immediately changes into a q1D ordered state in presence of finite Kitaev interactions. For both $\theta/\pi > 0.5$ and $\theta/\pi < 0.5$, the length of dipolar spin moments monotonically increases and behaves essentially the same as described for the 1D phase in the \mathbb{CP}^1 model in Sec. III C 1, where spins form dominant correlations along isolated 1D zigzag chains. The key distinction from the \mathbb{CP}^1 model lies in the presence of quadrupole correlations, which introduce weak interactions between the chains at very low temperatures. This leads to the formation of a 2D ordered state exhibiting one-dimensional character over a wide region at low and intermediate temperatures. This characteristic is the reason why we refer to the state as a quasi-1D state. Remarkably, quadrupole correlations stabilize the q1D phases in a wide region within the phase diagram, which is in stark contrast to the \mathbb{CP}^1 model, where the 1D phases remain stable only along a singular line. However, to this expense, the NC phases are notably suppressed, along with the neighboring TC phases.

In Fig. 8(b), we focus along the line at $\theta/\pi = 0.06$ [red line in Fig. 8(a)], and plot E/N_S and $\partial(E/N_S)/\partial\phi$ (top panel), the spin dipole norm $|\mathbf{S}|$ [see Eq. (10)] and quadrupole norm $|\mathbf{Q}|$ [see Eq. (11)] (middle panel), and the structure factors for dipoles, $S_S(\mathbf{q})$ [Eqs. (B3) and (B4)], and for quadrupoles,

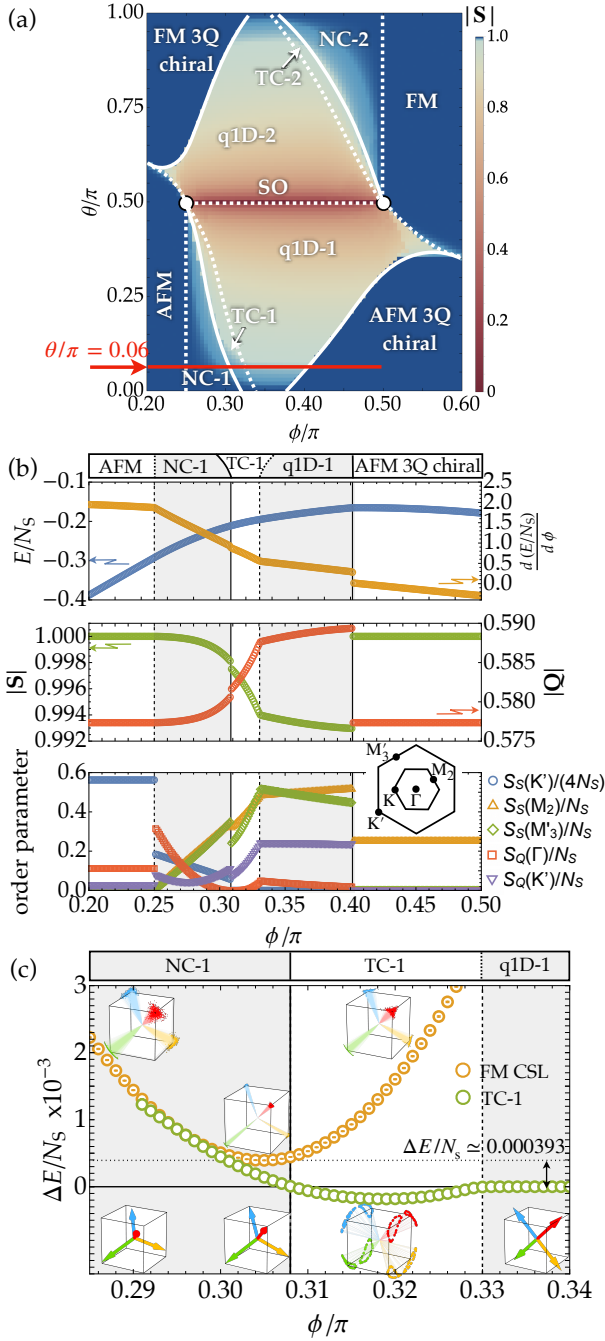


Figure 8. Competing phases of $\mathcal{H}_{\text{BBQ-K}}^A$ in Eq. (7) for $S = 1$ magnetic moments (\mathbb{CP}^2 model), obtained by variational energy minimization for a finite-size cluster of linear dimension $L = 120$ ($N_S = 28\,800$ spins) under periodic boundary conditions. (a) Averaged spin norm $|S|$ [see Eq. (10)] in the region $0.2 \leq \phi/\pi \leq 0.5$. The solid and dashed lines represent first- and second-order phase transitions, respectively. (b) The normalized energy E/N_S and its derivative $d(E/N_S)/d\phi$ (top panel), norms for dipole moment, $|S|$, and quadrupole moment, $|Q|$ [see Eq. (11)] (middle panel), and the structure factors for dipole moments, $S_S(\mathbf{q})$ [Eqs. (B3) and (B4)], and quadrupole moments, $S_Q(\mathbf{q})$ [Eqs. (B3) and (B5)] (bottom panel), along $\theta/\pi = 0.06$ [red line in (a)]. (c) Energy difference $\Delta E/N_S$, measured from the NC-1 state. The lower insets show spin configurations in each ordered phase, while the upper ones resemble metastable states of the FM CSL.

$S_Q(\mathbf{q})$ [Eqs. (B3) and (B5)], at relevant ordering vectors (bottom panel). We identify first-order phase transitions (solid lines) from NC-1 to TC-1 at $\phi/\pi = 0.3085(5)$, and from q1D-1 to AFM 3Q chiral at $\phi/\pi = 0.4015(1)$. Additionally, we find second-order transitions (dashed lines) from AFM to NC-1 at $\phi/\pi = 0.250(1)$, and from TC-1 to q1D-1 at $\phi/\pi = 0.3305(5)$. Notably, our measurements reveal a reduction in the spin dipole norm $|S| < 1$ within the NC-1, TC-1, and q1D-1 phases. It is worth noting that the reduction of $|S|$ is θ dependent; however, in this parameter region near the Kitaev limit, it is relatively small, with less than 1 %. This highlights the significance of dipole moments and justifies our comparison to the simplified \mathbb{CP}^1 model for dominant Kitaev interactions, as done in Sec. III C.

In Fig. 8(c), we present the energy difference between the metastable FM CSL and TC-1 states to the NC-1 ordered state. The presence of local quadrupole moments induces a small, yet finite energy difference to the FM CSL bounded by

$$\frac{\Delta E}{N_S} = 0.000393(4), \quad (38)$$

for $\phi/\pi = 0.305(1)$. Consequently, the CSL becomes an excited state rather than the ground state, with spin configurations no longer perfectly aligned with the corners of the unit cube, but still retaining the essential properties of the CSL as a metastable state. In fact, we find that the FM CSL is a metastable state with small energy gap in a wide region of the phase diagram, and smoothly merges with the AFM Kitaev SL for $\theta \rightarrow 0$ (see the Supplemental Material in Ref. [75]). The evolution of spin canting angles, illustrated in the bottom insets, closely resembles the general behavior discussed in the \mathbb{CP}^1 model [see Fig. 6(c)]. We note, however, a noticeable difference: At $\phi/\pi = 0.3085(5)$, the TC-1 state [see spin configurations in lower inset of Fig. 8(c)] becomes the ground state, a scenario which seems absent in the \mathbb{CP}^1 model. Furthermore, the q1D-1 state maintains its status as the ground state for $\phi/\pi > 0.3305(5)$, in contrast to the \mathbb{CP}^1 model where it remains the ground state only along a singular line.

2. Finite-temperature properties of \mathbb{CP}^2 model

The extensive degeneracy in the FM CSL and the small but finite energy gap to the ground state suggest that the system undergoes an entropy-driven phase transition from NC-1 order to the FM CSL at finite temperature. To confirm this, we show finite-temperature MC simulations for $\mathcal{H}_{\text{BBQ-K}}^A$ [Eq. (7)] in Fig. 9, for model parameters where the FM CSL shows the smallest energy difference to the ground state ($\theta/\pi = 0.06$ and $\phi/\pi = 0.305$). Figures 9(a)–9(d) are basically the same as those in Ref. [75], but we additionally show the static structure factors for quadrupoles $S_Q(\mathbf{q})$ in Fig. 9(e).

The specific heat C/N_S [Eq. (B1)] in Fig. 9(a) shows two singularities at $T_{c1} = 0.0055(2)$ and $T_{c2} = 0.0017(2)$, which scale weakly with system size. For $T \rightarrow 0$, we observe $C/N_S \rightarrow 2$, as expected for $S = 1$ magnetic moments described within the spin space of \mathbb{CP}^2 in the absence of soft-mode fluctuations [47]. Below T_{c2} , characteristic Bragg peaks

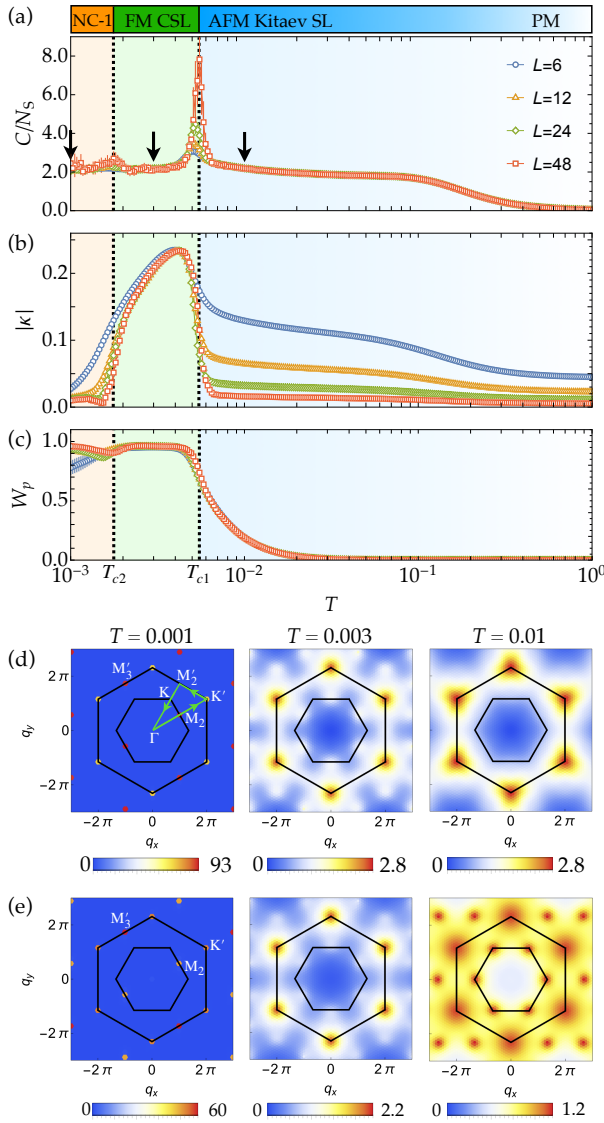


Figure 9. MC simulations of $\mathcal{H}_{\text{BBQ-K}}^A$ in Eq. (7), for the \mathbb{CP}^2 model at $\phi/\pi = 0.305$ and $\theta/\pi = 0.06$ reveal the presence of the FM CSL at finite temperatures. Shown are temperature dependencies of (a) the specific heat per site, C/N_S [Eq. (B1)], (b) the absolute value of the scalar spin chirality $|\kappa|$ [Eq. (B8)], and (c) the semiclassical analog of the \mathbb{Z}_2 -flux operator, W_p [Eq. (B14)]. Simulations were done for $L = 6, 12, 24$, and 48 ($N_S = 72, 288, 1152$, and 4608). (d) and (e) show the spin structure factor for dipoles, $S_S(\mathbf{q})$, and quadrupoles $S_Q(\mathbf{q})$ [Eqs. (B3)–(B5)], respectively, at temperatures indicated by black arrows in (a) for $L = 24$ at $T = 0.01$ and $T = 0.003$, while for $L = 12$ at $T = 0.001$. The green path in the left panel of (d) corresponds to the path used for the dynamical structure factor in Fig 10.

emerge in the structure factors at the momentum points, corresponding to the NC-1 order. Therefore, we associate T_{c2} with a symmetry-breaking transition into the NC-1 ordered phase [75].

The intermediate phase between T_{c1} and T_{c2} shows all properties of the FM CSL discussed in the previous subsec-

tions, namely a nonzero, size-independent scalar spin chirality $|\kappa|$ [Eq. (B8)], a value of W_p [Eq. (B14)] which is almost +1, and a very diffuse structure factor for spin dipoles, $S_S(\mathbf{q})$. The values of both quantities, $|\kappa|$ and W_p , are somewhat reduced compared to the ideal eight-color CSL discussed in Sec. III B. This reduction stems from the decrease in spin lengths $|\mathbf{S}|$ caused by the presence of small, but finite, quadrupole moments [see Fig. 8(b)] and temperature fluctuations.

The diffuse $S_S(\mathbf{q})$ is comparable to the structure factors found in the eight-color and \mathbb{CP}^1 models [see Figs. 4(j) and 7(d), respectively], albeit some additional weak intensity features around the M points in the first Brillouin zone. The quadrupole structure factor, $S_Q(\mathbf{q})$, also suggests the absence of quadrupolar order, with scattering patterns closely resembling those for dipoles. This similarity arises because spin moments are primarily dipolar in nature, and dipole characteristics are implicitly reflected in the quadrupole components. Taken these observations, we associate T_{c1} with a discrete chiral symmetry breaking into the FM CSL, as observed in the eight-color model and \mathbb{CP}^1 model cases [see Figs. 4(b) and 7(a), respectively]. It is worth noting that the intermediate-temperature CSL persists over an extended region around $\phi/\pi \approx 0.3$ and $\theta/\pi \approx 0.2$, as shown in the Supplemental Material of Ref. [75].

The scattering in $S_S(\mathbf{q})$ at $T = 0.01$, above T_{c1} , exhibits characteristics reminiscent of the semiclassical AFM Kitaev SL, as our chosen model parameters contain strong Kitaev interactions. The intensity exhibits diffuse accumulation around the Brillouin zone edge, similar to the results for the “pure” Kitaev model in Appendix E 1, however, with a stronger accumulation of diffuse intensity around the K' points. Meanwhile, the structure factor $S_Q(\mathbf{q})$ shows a more uniform intensity distribution with dominant scattering intensity around the K and K' points.

All physical observables characterizing the CSL in the \mathbb{CP}^2 model closely resemble those measured in the eight-color model (Sec. III B) and the \mathbb{CP}^1 model (Sec. III C). This remarkable consistency strongly suggests that the dominant properties of the CSL, as discussed in Sec. III B 1, remains robust even after considering all allowed local degrees of freedom for an $S = 1$ moment in the spin space \mathbb{CP}^2 . However, it is important to emphasize that the CSL no longer represents the ground state but emerges as an entropically driven state at finite temperature.

E. Dynamical properties of the chiral spin liquid

In this section we analyze dynamical properties of the CSL in the \mathbb{CP}^2 model. We show that the excitations corresponding to the CSL, in fact, are gapped, consistent with our observation of extreme short-range correlations in Fig. 5.

1. Excitation spectrum

In Fig. 10, we show the dynamical structure factors for spin-dipole moments, $\tilde{S}_S(\mathbf{q}, \omega)$ (top panels), and spin-quadrupole

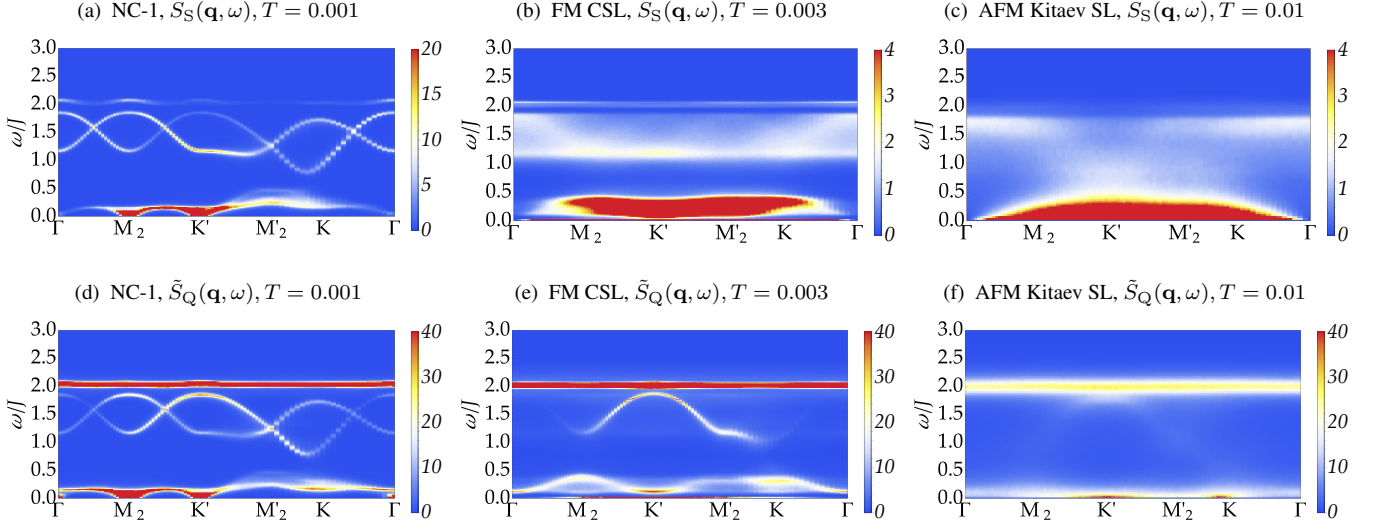


Figure 10. Dynamical structure factors [see Eqs. (B15)–(B17)] for spin-dipole moments, $\tilde{S}_S(\mathbf{q}, \omega)$ (top panels), and spin-quadrupole moments, $\tilde{S}_Q(\mathbf{q}, \omega)$ (bottom panels) of $\mathcal{H}_{\text{BBQ-K}}^A$ in Eq. (7), for the \mathbb{CP}^2 model, at $\phi/\pi = 0.305$ and $\theta/\pi = 0.06$. Results are shown for (a) and (d) the NC-1 ordered phase at $T = 0.001$, (b) and (e) the FM CSL at $T = 0.003$, and (c) and (f) the semiclassical analog of the AFM Kitaev SL at $T = 0.01$. Temperatures are indicated by black arrows in Fig. 9(a). Data were obtained from molecular dynamics simulations (details in Appendix A) for finite-size clusters of $L = 48$ ($N = 4608$). Results are plotted along the green path in momentum space, as indicated in the left panel of Fig. 9(d).

moments, $\tilde{S}_Q(\mathbf{q}, \omega)$ (bottom panels), which are obtained from molecular dynamics simulations (see details in Appendix A) at the same model parameters as chosen in Fig. 9. We show the spectrum along the path in momentum space, as indicated by green lines in the left panel of Fig. 9(d) and compare dynamics between the NC-1 ordered phase at $T = 0.001$, the FM CSL at $T = 0.003$, and the semiclassical analog of the AFM Kitaev SL at $T = 0.01$. Their corresponding equal-time structure factors are plotted in Figs. 9(d) and 9(e).

Figures 10(a) and 10(d) show the dynamical structure factors for the NC-1 ordered phase. For model parameters used here, the energy cost of a single-spin flip is primarily controlled by the Kitaev bond energies, limiting the bandwidth of excitations to $\omega/J \approx 2$. Given the magnetic order in this phase, well-defined spin waves and quadrupole waves emerge in the dipole and quadrupole channels, respectively. The signal reveals a nontrivial dispersion, which can be separated into three energy regimes. In the low-energy regime for $\omega/J \lesssim 0.5$, linearly dispersing Goldstone modes exist at the magnetic ordering vectors Γ , M_2 , and K' (M'_3 is not shown here), in accordance to the Bragg-peaks seen in the left column of Figs. 9(d) and 9(e). Moving to higher energy between $0.6 \lesssim \omega/J \lesssim 1.9$, two well-defined gapped bands exist, equally present in spin-dipole as well as spin-quadrupole channels. At the energy maximum, the spectrum features an almost flat band, corresponding to quadrupole excitations captured by strong intensity in $\tilde{S}_Q(\mathbf{q}, \omega)$. The band is almost flat, as the biquadratic interactions J_2 are small compared to the dominant Kitaev interactions K . A weak-intensity “shadow” of this excitation is visible in the dipole channel, coming from mixing between dipole and quadrupole excitations due

to spin-anisotropic interactions.

When the system turns into the FM CSL by increasing the temperature above T_{c2} , noticeable changes occur in the dynamical signatures, as shown in Figs. 10(b) and 10(e). The once well-defined spin waves at higher energy in the NC-1 ordered phase form a broad continuum of diffuse excitations with a gap of approximately $1.2J$ and a band maximum of around $1.9J$. We associate this continuum with the gapped excitations of the FM CSL. Considering the simplified eight-color model in Sec. III B, an elementary excitation out of the CSL ground-state manifold is comprised of a single-spin flip, violating the ground-state constraints in Fig. 2. However, such a single-spin flip will violate the ground-state constraints not only on one but on two bonds, with an energy cost on each bond of $\frac{2}{3}K$ [see Eq. (24)]. By using $K = \cos(0.06\pi)$, for the model parameters used in this calculation (see Fig. 9), we estimate a minimum excitation energy of

$$\Delta\omega_{\min}^{\text{CSL}} = 2 \times \frac{2}{3}K \approx 1.31J. \quad (39)$$

This estimate aligns well with the energy gap observed in Fig. 10(b). Above this energy region, quadrupole excitations do not form a continuum but instead exhibit well-defined quadrupole waves, with a remnant of one of the two branches seen in the NC-1 phase in Fig. 10(d). This is rather intriguing, since the energy-integrated correlations in Figs. 9(d) and 9(e) show a diffuse structure which is very similar for both $S_S(\mathbf{q})$ and $S_Q(\mathbf{q})$. This suggests that excitations in the CSL continuum induce coherent quadrupole dynamics at finite frequencies.

Furthermore, we observe that the well-defined Goldstone modes, corresponding to the NC-1 order change into a strong

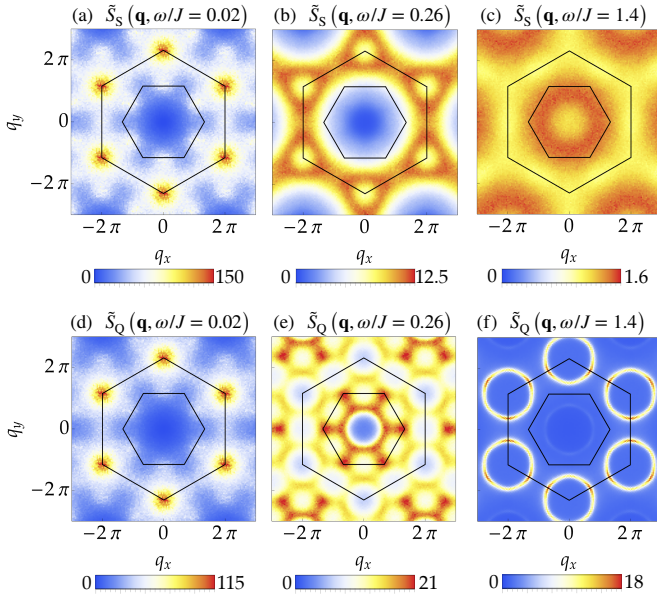


Figure 11. Energy cross sections of the dynamical structure factors [see Eqs. (B15)–(B17)] for the FM CSL phase in the \mathbb{CP}^2 model of $\mathcal{H}_{\text{BBQ-K}}^A$ [see Eq. (7)], as shown in Figs. 10(b) and 10(e). Results are shown in (a)–(c) for dipoles, $\tilde{S}_S(\mathbf{q}, \omega)$, while in (d)–(f) for quadrupoles, $\tilde{S}_Q(\mathbf{q}, \omega)$.

zero-energy flat band and a diffuse continuum of excitations with a small energy gap of $\sim 0.1J$ and bandwidth of $\sim 0.5J$. As the zero-energy mode is challenging to distinguish from the diffuse low-energy continuum, we provide the dynamics for the FM CSL in the \mathbb{CP}^1 model in Appendix E2. Here, dynamics exhibit more pronounced and sharper bands, allowing us to validate their genuine physical presence and ensuring that they are not artifacts of the simulations.

In Figs. 10(c) and 10(f), we show results above T_{c1} in the semiclassical analog of the AFM Kitaev SL. It appears that the three energy regimes observed in the FM CSL phase merge to form a spin structure factor that spans the full energy range up to $\omega/J \approx 2$, with strong intensity below $\sim 0.5J$. The quadrupole channel is dominated by an almost flat band at $\omega/J \approx 2$, which corresponds to the same excitations of quadrupolar origin as discussed in Figs. 10(d) and 10(e). The observed dynamical correlations in this finite-temperature phase strongly resemble the dynamics of the semiclassical Kitaev SL, as shown in the comparison in Appendix E1. This similarity supports our interpretation of a phase transition from the semiclassical Kitaev SL to the CSL state, since chosen model parameters ensure that Kitaev interactions strongly favor Kitaev SL physics above T_{c1} .

2. Energy cross sections

In the following, we examine the dynamical signatures in the FM CSL, shown in Figs. 10(b) and 10(e), at $T = 0.003$, in more detail by analyzing energy cross sections. In Fig. 11 we show dynamical structure factors [see Eqs. (B15)–(B17)]

for spin-dipole moments, $\tilde{S}_S(\mathbf{q}, \omega)$ (top panels) and spin-quadrupole moments, $\tilde{S}_Q(\mathbf{q}, \omega)$ (bottom panels) at particular energy values. The cross section at low energy, $\omega/J = 0.02$, in Figs. 11(a) and 11(d) shows a characteristic high-intensity, diffuse scattering signal with dominant weight around the K' points and some accumulation of weak spectral weight around the M points. These signals are almost completely captured by the equal-time structure factors $S_S(\mathbf{q})$ and $S_Q(\mathbf{q})$, shown in Figs. 9(d) and 9(e) (middle column).

At small, but finite energies, the spectrum shows a diffuse signal extending up to $\omega/J \approx 0.5$. An energy cross section within this energy range at $\omega/J = 0.26$ reveals complicated scattering features with finite intensity across the entire Brillouin zone. We observe dominant weight around the edge of the extended Brillouin zone for dipoles in Fig. 11(b), and predominant scattering within the first Brillouin zone for quadrupoles in Fig. 11(e).

The energy cross section within the diffuse and almost featureless continuum for spin dipoles at $\omega/J = 1.4$ reveals an almost uniform distribution of intensity over the entire Brillouin zone in Fig. 11(c). Within this energy range, where dipoles exhibit a continuum, quadrupole excitations display well-defined energy bands, as visible in Fig. 10(e). Shown in Fig. 11(f), these bands manifest as rings around the K' points in momentum space.

In Appendix E2, we explicitly compare the dynamical properties of the CSL in the \mathbb{CP}^2 model with the results obtained for the \mathbb{CP}^1 model. Our findings reveal a qualitative agreement between the two models, providing additional support for our interpretation that the spin liquid physics of the CSL is primarily governed by spin dipoles.

IV. SUMMARY AND PERSPECTIVES

In this paper, we explored the $S = 1$ Kitaev model with bilinear-biquadratic (BBQ) interactions on the honeycomb lattice for SU(3) spin-coherent states in the spin space \mathbb{CP}^2 , a model which hosts a diversity of exotic phases, including multiple- q states with nonzero scalar spin chirality, quasi-one-dimensional coplanar phases, twisted conical phases, and noncoplanar ordered states. Building upon the theory presented in our prior work, Ref. [75], our goal was to provide a pedagogical explanation of the nature and unique properties of a finite-temperature chiral spin liquid (CSL), apparent in this model. To achieve this, we utilized variational energy minimization and classical Monte Carlo (MC) with molecular dynamics simulations, using the recently developed U(3) formalism specifically designed for simulating $S = 1$ magnets [47].

By progressively restricting the spin degree of freedom from \mathbb{CP}^2 to \mathbb{CP}^1 and eventually to a discrete eight-color model, we unveiled the significant impact of the local Hilbert space dimension on the ground state and its excitation properties. The eight-color model, designed to capture the most intriguing aspects of the CSL, offered an intuitive and analytical understanding of its physical properties. This model not only uncovered the origin of the extensive degeneracy in the CSL,

but also clarified the reasons behind the nonzero scalar spin chirality, extreme short-ranged correlations, and the presence of a Kitaev spin liquid (SL) feature of \mathbb{Z}_2 -flux order. We derived bond-dependent spin constraints that unequivocally determine the nature of this eight-color CSL and validated our findings through unbiased classical MC simulations. Our results convincingly demonstrated that the dominant properties of the eight-color CSL persist even in the more complex \mathbb{CP}^1 and \mathbb{CP}^2 model cases. Importantly, the enlarged spin degree of freedom does not alter the fundamental properties of the CSL but rather restricts its stability in the ground state. Consequently, the CSL survives as an entropy-driven, robust phase at finite temperatures in the original \mathbb{CP}^2 model. This stability in the more complex \mathbb{CP}^2 model enabled us to simulate the dynamical structure factor, which revealed a nontrivial excitation spectrum characterized by a high-intensity zero-energy mode with a diffuse continuum of excitations in the low-frequency region. At higher frequencies, a broad continuum of excitations was observed, which we attributed to the excitations of the discrete eight-color CSL.

CSLs represent a well-established branch of SLs, wherein the SL state persists even after the spontaneous breaking of time-reversal symmetry [92, 93]. While examples of CSLs with exactly known quantum-ground states exist [94–97], studies across various models have indicated that the spontaneous breaking of discrete time-reversal symmetry typically occurs at finite temperatures [98–102]. The CSL investigated in our present study is a classical spin liquid that also spontaneously breaks time-reversal symmetry at finite temperature. We confirmed that this transition is of second order, following the \mathbb{Z}_2 Ising universality class. Remarkably, the correlations above and below this phase transition are strikingly similar [see Figs. 4(j) and 4(l)], suggesting a potential deeper connection to correlations seen in Kitaev SLs [90]. It would be intriguing to explore whether the nature of the phase transition in the \mathbb{CP}^1 and \mathbb{CP}^2 models exhibits similarities to the phase transition observed in the eight-color model, and whether such behavior could also be found in other lattice models which host classical CSLs [103]. Furthermore, the defining bond-dependent spin constraints, as illustrated in Fig. 2, can be expressed in terms of a suitable lattice gauge theory [104]. This directly leads to the intriguing question of whether the CSL can also exist on other three-coordinated lattices with different geometries and whether there is a potential relevance to compass models [105]. We leave these intriguing questions for future work.

We strongly advocate for simulating systems with higher-order interactions within their corresponding local Hilbert space dimension. While it may be theoretically straightforward to formulate and solve models with any type of spin interactions, it is crucial to ensure that the local Hilbert space respects the underlying Lie algebra, which physically allows for such interactions [49, 106]. For instance, biquadratic interactions, J_2 , are absent for spin moments described by Pauli matrices in the $\mathfrak{su}(2)$ Lie algebra. To address such interactions in a physically realistic setting, it is necessary to formulate the problem in $SU(3)$, with generators in form of Gell-Mann matrices. To illustrate the profound impact of changing

the local spin degree of freedom, our results in Fig. 1 provide a compelling demonstration using a specific example. Also other examples, such as the BBQ model on the triangular lattice, reveal very different properties for spins living in \mathbb{CP}^1 (classical Heisenberg spins) [107, 108], compared to spins in \mathbb{CP}^2 [24, 39, 47]. In particular, realistic Mott insulators, in their effective low-energy description, can accommodate hybridized multipole moments, which can be efficiently studied within their corresponding $SU(N)$ representation [50, 109].

The $U(3)$ formalism [47] has been used in the present paper as a semiclassical approximation that neglects quantum entanglement between different sites. A very promising and important direction for future studies would involve the treatment of the same model with methods which can account for long-range entanglement. In such a case, we expect that quantum fluctuations will broaden the Kitaev SL phases, which, in our semiclassical simulations, are confined to the singular Kitaev points located at the north and south poles of the phase diagram in Fig. 1. In fact, this expectation has already been realized by recent iPEPS studies in Ref. [110], which examined the unfrustrated regime of the $S = 1$ BBQ-Kitaev model for $1 < \phi/\pi < 2$ [cf. Fig. 1(a)]. Moreover, recent work utilizing DMRG techniques on the $S = 1$ Kitaev model has identified the emergence of chiral ordered phases in the presence of symmetric off-diagonal interactions [111] and vortex states in the presence of single-ion anisotropy [112]. These findings provide intriguing results that underscore the richness of the quantum problem, offering promising avenues for further exploration. Furthermore, given that the CSL phases in the \mathbb{CP}^2 model persist at finite temperatures in close proximity to the Kitaev points, it might be possible that quantum fluctuations will stabilize the CSL phases even in the ground state. This raises the possibility of an intriguing connection to Schwinger boson mean-field theory, which proposes the existence of a gapped chiral QSL [113]. Additionally, it is known that the SO phase in the BBQ model will transform into a plaquette valence bond solid (pVBS), as observed from iPEPS simulations [88]. It would be interesting to investigate how far the pVBS extends in the presence of Kitaev interactions and whether the one-dimensional phase (1D/q1D) survives in this scenario or not. If such a phase persists in a quantum simulation, it could potentially stabilize exotic phases like the Haldane phase [114], quantum loop states [115], or other phases with dimensionally reduced characteristics, as observed in anisotropic $S = 1/2$ Kitaev models [116, 117].

The $S = 1$ Kitaev model with BBQ interactions offers a diverse range of interesting and exotic phases. In the Kitaev limit we recovered the semiclassical analog of the $S = 1$ Kitaev SL, as suggested for honeycomb materials with Ni^{2+} ions [72]. However, when considering the experimental realization of higher- S Kitaev materials, it becomes apparent that achieving ideal interactions poses significant challenges. $S = 1$ magnets naturally introduce higher-order biquadratic interactions, placing potential candidate materials likely in the vicinity of the Kitaev limit, but with finite J_1 and J_2 interactions. In such cases, the surrounding phases become relevant for characterizing and classifying synthesized materials. A ferroquadrupolar spin nematic state is expected for negative

biquadratic interactions, J_2 , which can be expected in materials with spin-phonon coupling [118]. States, such as triple- q , q1D, and CSL states appear for positive biquadratic interactions J_2 , which are expected in materials with orbital degeneracy [119–121]. Phases with scalar spin chirality, such as the FM/AFM CSL or triple- q ordered states found in this study, are of particular interest, as they may lead to unconventional phenomena, such as the magnon Hall effect [122–124]. In fact, triple- q states were also found in the Kitaev-Heisenberg model under magnetic field [125] and play a crucial role in understanding the physics of materials such as the honeycomb cobaltites $\text{Na}_2\text{Co}_2\text{TeO}_6$ [126, 127], and $\text{Na}_3\text{Co}_2\text{SbO}_6$ [128]. Despite the presence of non-Kitaev interactions, the CSL presented in our study is stable at finite temperatures in the vicinity of the Kitaev limit. This observation suggests the intriguing possibility of stabilizing a similar state in real materials, potentially leading to the emergence of a novel Kitaev-like SL that breaks time-reversal symmetry.

ACKNOWLEDGMENTS

The authors are pleased to acknowledge helpful conversations with Cristian Batista, Matthias Gohlke, Yasuyuki Kato, Geet Rakala, Kotaro Shimizu, and Han Yan. This work was supported by the Quantum Liquid Crystals JSPS KAKENHI Grants No. JP19H05822 and No. JP19H05825, MEXT as "Program for Promoting Research on the Supercomputer Fugaku" (Grant No. JPMXP1020230411), and the Theory of Quantum Matter Unit, OIST. Numerical calculations were carried out using HPC facilities provided by the Supercomputer Center of the Institute for Solid State Physics, the University of Tokyo.

Appendix A: Details of methods

In this Appendix, we describe the numerical methods used in this study. Simulations are performed for different spin degrees of freedom, namely, $\text{SU}(3)$ spin-coherent states on the complex-projective plane \mathbb{CP}^2 , $\text{SU}(2)$ spin-coherent states on \mathbb{CP}^1 , and discretized spins in the eight-color model. Energies in each case are evaluated at the level of classical approximations on local bonds, and hence do not allow us to treat long-range quantum entanglement beyond a single site.

1. Variational energy minimization

To determine the ground-state phase diagrams, as shown in Fig. 1, we perform large-scale variational energy minimization using the machine learning library JAX [80]. In Fig. 1(a) we minimize $\mathcal{H}_{\text{BBQ-K}}^A$ in Eq. (7) by optimizing θ_1 , θ_2 , ϕ_1 , ϕ_2 and ϕ_3 in Eq. (6) as independent variational parameters at each site on the lattice. Similarly, in Fig. 1(b) we minimize $\mathcal{H}_{\text{BBQ-K}}^S$ in Eq. (1) using local variational parameters θ_1 and ϕ_1 in Eq. (14). We employ the gradient processing and optimization library “Optax” with the optimizer “Adam” [81].

The initial conditions considered include relevant ordered and disordered states, as depicted in Fig. 1(d), as well as random initial states. The optimization process involves 5000-10000 steps per model parameter.

2. Monte Carlo simulation

To obtain thermodynamic properties we perform classical MC simulations where spins are locally updated at every site on the physical lattice of size N_S . In the \mathbb{CP}^2 spin space, we sample \mathcal{A} matrices by choosing parameters $0 \leq \theta_1, \theta_2 \leq 1$ and $0 \leq \phi_1, \phi_2 < 2\pi$ in Eq. (6) at random, while in the \mathbb{CP}^1 spin space we sample classical vector spins with $-1 \leq \cos \theta_1 \leq 1$ and $0 \leq \phi_1 < 2\pi$ in Eq. (14). For a spin flip in the eight-color model we randomly select, with equal weight, one out of all eight possible spin states, as defined in Table I. Following the standard single-spin flip Metropolis algorithm [129] we accept or reject a new spin state at site i , after evaluating the local bond energies. In the actual calculations, a single MC step consists of N_S local spin-flip attempts on randomly chosen sites. Simulations are carried out in parallel for replicas at different temperatures, using the replica-exchange method, initiated by the parallel tempering algorithm [130–132] every 100 MC steps. Results for thermodynamic quantities are averaged over 5×10^5 statistically independent samples, after initial 5×10^5 MC steps for slowly heating from the ground state, as obtained by the variational energy minimization and further 5×10^5 MC steps for thermalization. Error bars are estimated by averaging over 10 independent simulation runs.

MC simulations in the frustrated parameter region, where the eight-color CSL appears, suffer from severe slowing down, due to the failure of single-spin flip updates. As explained in Sec III B 1, the CSL is expected to have an extensive number of degenerate states, which are connected via simultaneous flips of a group of spins covering at least one hexagon (see Fig. 3). To efficiently sample over an extensive manifold of states, we combine single-spin flip updates with an additional cluster update of six spins. For the eight-color model and the \mathbb{CP}^1 model we adopt Eq. (28), while for the \mathbb{CP}^2 model, where spins are represented by 3×3 Hermitian \mathcal{A} -matrices [see Eqs. (3)–(6)], we transform Eq. (28) into the matrix form

$$\mathcal{A}_{p,j}^{\text{new}} = (R_j^\alpha)^{-1} \mathcal{A}_{p,j} R_j^\alpha. \quad (\text{A1})$$

By comparing energies before and after the cluster update, we accept or reject the new state following the Metropolis argument [129]. Within one MC step we implement $N_h = N_S/2$ cluster-update attempts for randomly chosen hexagons on the whole lattice. The efficiency of this update within the CSL phase strongly depends on the degrees of freedom of spins. As discussed for the acceptance ratio in Appendix D, this cluster update becomes rejection free in the eight-color model, while showing a reduced efficiency for \mathbb{CP}^1 and \mathbb{CP}^2 model calculations.

3. Molecular dynamics simulation

Dynamics are present in models with continuous spin degree of freedom, here in our case for the \mathbb{CP}^2 and \mathbb{CP}^1 models. The equations of motion for spins respecting the spin space \mathbb{CP}^2 [spin coherent states of $SU(3)$] are expressed within our formalism in terms of \mathcal{A} matrices (see Sec. II). This allows us to rewrite the original BBQ-Kitaev Hamiltonian in Eq. (1) into the bilinear form of Eq. (7),

$$\mathcal{H}_{\text{BBQ-K}}^{\mathcal{A}} = \mathcal{H}_{\text{BBQ}}^{\mathcal{A}} + \mathcal{H}_{\text{K}[x]}^{\mathcal{A}} + \mathcal{H}_{\text{K}[y]}^{\mathcal{A}} + \mathcal{H}_{\text{K}[z]}^{\mathcal{A}} \quad (\text{A2})$$

with

$$\mathcal{H}_{\text{BBQ}}^{\mathcal{A}} = \sum_{\langle ij \rangle} \left[J_1 \mathcal{A}_{i\beta}^{\alpha} \mathcal{A}_{j\alpha}^{\beta} + (J_2 - J_1) \mathcal{A}_{i\beta}^{\alpha} \mathcal{A}_{j\beta}^{\alpha} + J_2 \mathcal{A}_{i\alpha}^{\alpha} \mathcal{A}_{j\beta}^{\beta} \right], \quad (\text{A3})$$

$$\mathcal{H}_{\text{K}[x]}^{\mathcal{A}} = -K_x \sum_{\langle ij \rangle_x} (\mathcal{A}_{iz}^y - \mathcal{A}_{iy}^z) (\mathcal{A}_{jz}^y - \mathcal{A}_{jy}^z), \quad (\text{A4})$$

$$\mathcal{H}_{\text{K}[y]}^{\mathcal{A}} = -K_y \sum_{\langle ij \rangle_y} (\mathcal{A}_{iz}^x - \mathcal{A}_{ix}^z) (\mathcal{A}_{jz}^x - \mathcal{A}_{jx}^z), \quad (\text{A5})$$

$$\mathcal{H}_{\text{K}[z]}^{\mathcal{A}} = -K_z \sum_{\langle ij \rangle_z} (\mathcal{A}_{iy}^x - \mathcal{A}_{ix}^y) (\mathcal{A}_{jy}^x - \mathcal{A}_{jx}^y), \quad (\text{A6})$$

where \mathcal{A} matrices respect the commutation relations [47]:

$$[\mathcal{A}_{i\eta}^{\alpha}, \mathcal{A}_{i\eta}^{\gamma}] = \delta_{\beta}^{\gamma} \mathcal{A}_{i\eta}^{\alpha} - \delta_{\eta}^{\alpha} \mathcal{A}_{i\eta}^{\gamma}, \quad [\mathcal{A}_{i\beta}^{\alpha}, \mathcal{A}_{i\eta}^{\gamma}] = 0. \quad (\text{A7})$$

By using Eq. (A7), one can solve the Heisenberg equations of motion, written in terms of \mathcal{A} matrices

$$\frac{d}{dt} \mathcal{A}_{i\beta}^{\alpha} = \frac{d}{dt} \mathcal{A}_{i\beta}^{\alpha} \Big|_{\text{BBQ}} + \frac{d}{dt} \mathcal{A}_{i\beta}^{\alpha} \Big|_{\text{K}[x]} + \frac{d}{dt} \mathcal{A}_{i\beta}^{\alpha} \Big|_{\text{K}[y]} + \frac{d}{dt} \mathcal{A}_{i\beta}^{\alpha} \Big|_{\text{K}[z]}, \quad (\text{A8})$$

which can be explicitly solved for contributions from the BBQ interactions

$$\begin{aligned} \frac{d}{dt} \mathcal{A}_{i\beta}^{\alpha} \Big|_{\text{BBQ}} &= -i [\mathcal{A}_{i\beta}^{\alpha}, \mathcal{H}_{\text{BBQ}}^{\mathcal{A}}] \\ &= -i \sum_{\delta} \left[J_1 \left(\mathcal{A}_{i\gamma}^{\alpha} \mathcal{A}_{i+\delta,\beta}^{\gamma} - \mathcal{A}_{i\beta}^{\gamma} \mathcal{A}_{i+\delta,\gamma}^{\alpha} \right) \right. \\ &\quad \left. + (J_2 - J_1) \left(\mathcal{A}_{i\gamma}^{\alpha} \mathcal{A}_{i+\delta,\gamma}^{\beta} - \mathcal{A}_{i\beta}^{\gamma} \mathcal{A}_{i+\delta,\alpha}^{\gamma} \right) \right], \end{aligned} \quad (\text{A9})$$

where \sum_{δ} sums over the nearest neighbors of site i . For the bond-dependent Kitaev interactions, e.g., on the x bond we obtain

$$\begin{aligned} \frac{d}{dt} \mathcal{A}_{i\beta}^{\alpha} \Big|_{\text{K}[x]} &= -i [\mathcal{A}_{i\beta}^{\alpha}, \mathcal{H}_{\text{K}[x]}^{\mathcal{A}}] \\ &= iK_x [\mathcal{A}_{i\beta}^{\alpha}, (\mathcal{A}_{iz}^y - \mathcal{A}_{iy}^z)] (\mathcal{A}_{i+x,z}^y - \mathcal{A}_{i+x,y}^z) \\ &= iK_x \left(\delta_{i\beta}^y \mathcal{A}_{iz}^{\alpha} - \delta_{i\beta}^z \mathcal{A}_{iy}^{\alpha} - \delta_{\beta}^z \mathcal{A}_{i\gamma}^{\alpha} + \delta_{\gamma}^y \mathcal{A}_{i\beta}^{\alpha} \right) \\ &\quad \times (\mathcal{A}_{i+x,z}^y - \mathcal{A}_{i+x,y}^z), \end{aligned} \quad (\text{A10})$$

which explicitly gives

$$\left. \begin{aligned} \frac{d}{dt} \mathcal{A}_{iy}^{\alpha} \Big|_{\text{K}[x]} &= \mathcal{A}_{iz}^{\alpha} \\ \frac{d}{dt} \mathcal{A}_{iz}^{\alpha} \Big|_{\text{K}[x]} &= -\mathcal{A}_{iy}^{\alpha} \\ \frac{d}{dt} \mathcal{A}_{i\beta}^y \Big|_{\text{K}[x]} &= \mathcal{A}_{i\beta}^z \\ \frac{d}{dt} \mathcal{A}_{i\beta}^z \Big|_{\text{K}[x]} &= -\mathcal{A}_{i\beta}^y \end{aligned} \right\} \times iK_x (\mathcal{A}_{i+x,z}^y - \mathcal{A}_{i+x,y}^z). \quad (\text{A11})$$

Contributions on the y and z bonds can be obtained by cyclic permutations.

The equations of motion for spins respecting the spin space \mathbb{CP}^1 [spin coherent states of $SU(2)$] are formulated in terms of classical Heisenberg spins, see Eq. (14). We obtain from Eq. (1) the equations of motion

$$\begin{aligned} \frac{d}{dt} \mathbf{S}_i^{\alpha} &= -i [\mathbf{S}_i^{\alpha}, \mathcal{H}_{\text{BBQ}}^{\mathcal{S}}] \\ &= -iJ_1 \sum_{\langle ij \rangle} [\mathbf{S}_i^{\alpha}, (\mathbf{S}_i \cdot \mathbf{S}_j)] \\ &\quad - 2iJ_2 \sum_{\langle ij \rangle} [\mathbf{S}_i^{\alpha}, (\mathbf{S}_i \cdot \mathbf{S}_j)] (\mathbf{S}_i \cdot \mathbf{S}_j) \\ &\quad - i \sum_{\langle ij \rangle_{\gamma}} K_{\gamma} [\mathbf{S}_i^{\alpha}, \mathbf{S}_i^{\gamma} \mathbf{S}_j^{\gamma}], \end{aligned} \quad (\text{A12})$$

which explicitly gives

$$\frac{d}{dt} \mathbf{S}_i = \mathbf{S}_i \times \sum_{\delta} \{ [J_1 + 2J_2 (\mathbf{S}_i \cdot \mathbf{S}_{i+\delta})] \mathbf{S}_{i+\delta} + K_{\delta} \mathbf{S}_{i+\delta}^{\delta} \}, \quad (\text{A13})$$

where “ \times ” corresponds to the cross product between vector spins on the left and the local exchange field on the right. Throughout this article we choose isotropic Kitaev interactions with $K_x = K_y = K_z = K$.

After sufficient thermalization at a specific temperature with MC simulations we evolve 1000 statistically independent \mathcal{A} -matrix (\mathbf{S} vector) configurations in time by numerically integrating the equations of motion using a fourth-order Runge-Kutta (RK-4) algorithm [133, 134]. By using a time interval of $\delta t \approx 0.03$, we obtain a time series of \mathcal{A} matrices, $\{\mathcal{A}_{i\beta}^{\alpha}(t)\}$, and classical vectors, $\{\mathbf{S}_i(t)\}$, which conserve the total energy of the system with a controlled error of $\mathcal{O}(\delta t^5)$, as expected from the RK-4 method.

Appendix B: Measurement of observables

1. Specific heat and entropy

During the MC measurement, we compute the specific heat

$$C = \frac{1}{k_B T^2} [\langle \mathcal{H}^2 \rangle - \langle \mathcal{H} \rangle^2], \quad (\text{B1})$$

where $k_B = 1$ throughout this paper, and $\langle \dots \rangle$ represents an average over measurements of statistically-independent

replica. In the discretized eight-color model we obtain the thermodynamic entropy, by integrating the specific heat over the temperature

$$S(T) = S(T_\infty) - \int_T^{T_\infty} \frac{C(T')}{T'} dT', \quad (\text{B2})$$

with T_∞ the highest temperature available.

2. Correlations in momentum space

Correlations between magnetic moments in momentum space are accessible from the equal-time structure factor

$$S_\lambda(\mathbf{q}) = \left\langle \sum_{\alpha\beta} |m_{\lambda\alpha\beta}(\mathbf{q})|^2 \right\rangle, \quad (\text{B3})$$

where the index λ denotes the channel for \mathcal{A} matrices, dipoles, or quadrupoles as $\lambda = \mathcal{A}, S$, and Q , respectively. Here, $m_{\lambda\alpha\beta}(\mathbf{q})$ is defined by

$$m_S^\alpha(\mathbf{q}) = -i \sum_{\beta,\gamma} \epsilon_{\beta\gamma}^\alpha m_{\mathcal{A}\gamma}(\mathbf{q}), \quad (\text{B4})$$

$$m_Q^\alpha(\mathbf{q}) = -m_{\mathcal{A}\beta}^\alpha(\mathbf{q}) - m_{\mathcal{A}\alpha}^\beta(\mathbf{q}) + \frac{2}{3} \delta_{\beta}^\alpha \sum_{\gamma} m_{\mathcal{A}\gamma}(\mathbf{q}), \quad (\text{B5})$$

where the Fourier transform of the \mathcal{A} matrices is given as

$$m_{\mathcal{A}\beta}^\alpha(\mathbf{q}) = \frac{1}{\sqrt{N_S}} \sum_i e^{i\mathbf{q}\cdot\mathbf{r}_i} \mathcal{A}_{i\beta}^\alpha. \quad (\text{B6})$$

For simulations in the \mathbb{CP}^1 model and the eight-color model, we evaluate dipole correlations directly

$$m_S^\alpha(\mathbf{q}) = \frac{1}{\sqrt{N_S}} \sum_i e^{i\mathbf{q}\cdot\mathbf{r}_i} S_i^\alpha, \quad (\text{B7})$$

from spin components sampled via Eq. (14).

3. Scalar spin chirality and semiclassical \mathbb{Z}_2 -flux operator

We define the scalar spin chirality on the honeycomb lattice with

$$\kappa = \frac{2}{N_S} \sum_p \kappa_p, \quad (\text{B8})$$

where the sum is taken over all hexagons p . As shown in Fig. 12(a) we divide a single hexagon into four triangles which contribute to the total scalar chirality of the full hexagon with

$$\kappa_p = \kappa_p^A + \kappa_p^B + \kappa_p^C + \kappa_p^D, \quad (\text{B9})$$

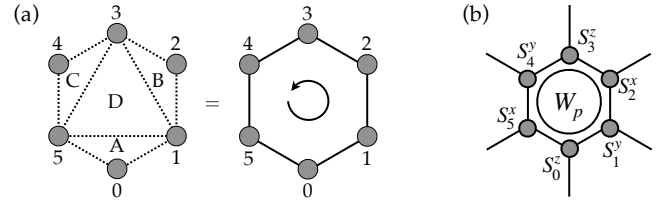


Figure 12. (a) Definition of the scalar spin chirality on an individual hexagon, see Eqs. (B9)–(B13). (b) The semiclassical analog of the \mathbb{Z}_2 -flux operator, as defined in Eq. (B14).

where

$$\kappa_p^A = \mathbf{S}_{p0} \cdot (\mathbf{S}_{p1} \times \mathbf{S}_{p5}), \quad (\text{B10})$$

$$\kappa_p^B = \mathbf{S}_{p1} \cdot (\mathbf{S}_{p2} \times \mathbf{S}_{p3}), \quad (\text{B11})$$

$$\kappa_p^C = \mathbf{S}_{p3} \cdot (\mathbf{S}_{p4} \times \mathbf{S}_{p5}), \quad (\text{B12})$$

$$\kappa_p^D = \mathbf{S}_{p1} \cdot (\mathbf{S}_{p3} \times \mathbf{S}_{p5}). \quad (\text{B13})$$

We further define the $S = 1$ semiclassical analog of the “ \mathbb{Z}_2 -flux” operator, W_p , as

$$W_p = \prod_{j \in p} \sqrt{3} S_j^\alpha, \quad (\text{B14})$$

where α denotes the site-dependent label for the Kitaev bond pointing outwards from the hexagon p at site $j = 0, \dots, 5$. Figure 12(b) visually represents Eq. (B14), which, in MC simulations, is computed as the spatial average over all plaquettes on the lattice. We emphasize that W_p differs from the conserved flux operator in the quantum $S = 1$ Kitaev model [57, 76].

4. Dynamical structure factor

To obtain the dynamical structure factors for dipole and quadrupole channels, we take the Fourier transform of the time-series of \mathcal{A} matrices $\{\mathcal{A}_{i\beta}^\alpha(t)\}$ (classical vectors $\{\mathbf{S}_i(t)\}$), as obtained from molecular dynamics simulations (see Appendix A3), from real-space into the momentum-space and frequency domain

$$S_\lambda(\mathbf{q}, \omega) = \left\langle \sum_{\alpha\beta} |m_{\lambda\alpha\beta}(\mathbf{q}, \omega)|^2 \right\rangle, \quad (\text{B15})$$

with $\lambda = \mathcal{A}, S$, and Q . The Fourier transform

$$m_{\mathcal{A}\beta}^\alpha(\mathbf{q}, \omega) = \frac{1}{\sqrt{N_t}} \sum_n e^{i\omega t_n} m_{\mathcal{A}\beta}^\alpha(\mathbf{q}, t_n), \quad (\text{B16})$$

for \mathcal{A} matrices is obtained by the fast Fourier transform (FFT) [135], after convoluting with a Gaussian envelope to avoid numerical artifacts like the Gibbs phenomenon [136]. Equivalent equations for dipole moments, $m_S^\alpha(\mathbf{q}, \omega)$, and quadrupole moments, $m_Q^\alpha(\mathbf{q}, \omega)$, are defined in analogy to Eqs. (B4) and (B5), respectively.

In Figs. 10, 11, and Appendix E 2, we set the total number of time steps $N_t = 500$ for a maximal frequency of $\omega_{\max} = 10J$, while in Appendix E 1, we set $\omega_{\max} = 6J$. Data are sampled over 1000 statistically independent time series.

The Heisenberg equations of motion [see Eqs. (A8)–(A10) and Eq. (A13)] are derived using bosonic commutation relations [c.f. Eq. (A7)], resulting in a dispersion relation analogous to those found in flavor-wave theory [47]. However, the molecular dynamics simulations described above are performed for a thermal ensemble of classical states, evolving in time while adhering to the bosonic commutation relations. This effectively leads to dynamics of a “mixed ensemble”, encompassing classical and bosonic statistics.

To obtain a dynamical structure factor that adheres strictly to quantum statistics, it is necessary to introduce a prefactor ω/T , which allows to “correct” the intensity distribution via

$$\tilde{S}_\lambda(\mathbf{q}, \omega) = \frac{\omega}{T} S_\lambda(\mathbf{q}, \omega), \quad (\text{B17})$$

as discussed in great detail in Sec. VII of Ref. [47], and the Supplemental Material of Ref. [137]. Throughout the present paper, all dynamical structure factors are presented in their “corrected” form, $\tilde{S}_\lambda(\mathbf{q}, \omega)$.

Appendix C: Analytic solutions of phase boundaries for CSL

In this Appendix we provide an analytical derivation for the phase boundaries of the FM CSL in the ground state of the eight-color model, and in the \mathbb{CP}^1 model, as discussed in Sec. III A.

1. CSL phase at singular line in the \mathbb{CP}^1 model

In the following we derive the singular line in the phase diagram where the FM CSL becomes the ground state in the \mathbb{CP}^1 model, $\mathcal{H}_{\text{BBQ-K}}^S$ in Eq. (1), see Fig. 1(b). Without loss of generality, we consider one possible arrangement of spins in the FM CSL ground state with nearest-neighbors ($\mathbf{S}_g, \mathbf{S}_r$) on the x bond, ($\mathbf{S}_g, \mathbf{S}_b$) on the y bond, and ($\mathbf{S}_g, \mathbf{S}_r$) on the z bond, which all respect the bond-dependent spin constraints of Fig. 2. We hereby follow the convention of spin states as defined in Table I for the eight-color states.

We first consider the energy contribution from bilinear interactions, J_1 , and biquadratic interactions, J_2 . These are bond independent, which is why we consider energies only on the x bond for simplicity. By parametrizing spins on the Bloch sphere [see Eq. (14)], with, e.g., θ_g and ϕ_g , the polar and azimuthal angles of a “green” spin, we write:

$$\mathbf{S}_g \cdot \mathbf{S}_r = \sin \theta_g \sin \theta_r \cos(\phi_g - \phi_r) + \cos \theta_g \cos \theta_r = -\frac{1}{3}, \quad (\text{C1})$$

and

$$\begin{aligned} (\mathbf{S}_g \cdot \mathbf{S}_r)^2 &= [\sin \theta_g \sin \theta_r \cos(\phi_g - \phi_r)]^2 + [\cos \theta_g \cos \theta_r]^2 \\ &\quad + \sin \theta_g \sin \theta_r \cos \theta_g \cos \theta_r \cos(\phi_g - \phi_r) \\ &= \frac{1}{9}. \end{aligned} \quad (\text{C2})$$

Considering the spin $\tilde{\mathbf{S}}_g$, after allowing for a small perturbation in θ_g by $\delta \ll 1$, gives

$$\begin{aligned} \tilde{\mathbf{S}}_g \cdot \mathbf{S}_r &= \mathbf{S}_g \cdot \mathbf{S}_r - \delta \sin \theta_g \cos \theta_r \\ &= \mathbf{S}_g \cdot \mathbf{S}_r - \frac{\sqrt{2}}{3} \delta. \end{aligned} \quad (\text{C3})$$

Equivalently we obtain:

$$\begin{aligned} (\tilde{\mathbf{S}}_g \cdot \mathbf{S}_r)^2 &= (\mathbf{S}_g \cdot \mathbf{S}_r - \delta \sin \theta_g \cos \theta_r)^2 \\ &= (\mathbf{S}_g \cdot \mathbf{S}_r)^2 - 2(\mathbf{S}_g \cdot \mathbf{S}_r) \delta \sin \theta_g \cos \theta_r + \mathcal{O}(\delta^2) \\ &= (\mathbf{S}_g \cdot \mathbf{S}_r)^2 + \frac{2}{3} \frac{\sqrt{2}}{3} \delta, \end{aligned} \quad (\text{C4})$$

where we neglect terms of higher order $\mathcal{O}(\delta^2)$.

The energies from bond-dependent Kitaev interactions contribute on the x bond:

$$\begin{aligned} \tilde{\mathbf{S}}_g \cdot \mathbf{S}_r &= \mathbf{S}_g \cdot \mathbf{S}_r - \delta \cos \theta_g \cos \phi_g \sin \theta_r \cos \phi_r \\ &= \mathbf{S}_g \cdot \mathbf{S}_r + \frac{\delta \sqrt{2}}{2} \frac{1}{3}, \end{aligned} \quad (\text{C5})$$

on the y bond:

$$\begin{aligned} \tilde{\mathbf{S}}_g \cdot \mathbf{S}_b &= \mathbf{S}_g \cdot \mathbf{S}_b + \delta \cos \theta_g \sin \phi_g \sin \theta_b \sin \phi_b \\ &= \mathbf{S}_g \cdot \mathbf{S}_b + \frac{\delta \sqrt{2}}{2} \frac{1}{3}, \end{aligned} \quad (\text{C6})$$

and on the z bond:

$$\begin{aligned} \tilde{\mathbf{S}}_g \cdot \mathbf{S}_r &= \mathbf{S}_g \cdot \mathbf{S}_r - \delta \sin \theta_g \cos \theta_r \\ &= \mathbf{S}_g \cdot \mathbf{S}_r - \delta \frac{\sqrt{2}}{3}. \end{aligned} \quad (\text{C7})$$

The energy difference, ΔE , between the CSL ground state and a state with small perturbation, using Eqs. (C3)–(C7), is

$$\Delta E = \frac{\sqrt{2}}{3} \delta \left(-J_1 + \frac{2}{3} J_2 \right) + K \delta \left(\frac{1}{2} \frac{\sqrt{2}}{3} + \frac{1}{2} \frac{\sqrt{2}}{3} - \frac{\sqrt{2}}{3} \right). \quad (\text{C8})$$

Thus, the CSL ground state is realized when $\Delta E = 0$, which occurs for

$$J_1 = \frac{2}{3} J_2. \quad (\text{C9})$$

This condition corresponds to the model parameters, defined in Eq. (2)

$$\phi/\pi = \frac{1}{\pi} \arctan \left(\frac{3}{2} \right) \approx 0.312833, \quad (\text{C10})$$

as found from numerics in Fig. 1(b), and stated in Eq. (16). Since the contributions from Kitaev energies perfectly cancel out, the CSL phase forms a singular straight line in the phase diagram. A similar energy comparison can be applied to the AFM CSL phase, leading to Eq. (17).

2. Phase boundaries of CSL in the eight-color model

The phase boundaries of the FM CSL phase in the eight-color model, $\mathcal{H}_{\text{BBQ-K}}^{8c}$ in Eq. (15), can also be calculated analytically. The FM CSL is surrounded by the AFM and AFM 3Q chiral ordered phases [see Fig. 1(c)]. Without loss of generality, we consider the local-bond energy for only one bond in the lattice, here the x bond.

In the FM CSL, by respecting the bond-dependent spin constraints in Fig. 2, one obtains for allowed nearest-neighbors, e.g., “bright green” and “bright red”, the local bond energy $\sigma_g \cdot \sigma_r = -1/3$. On the other side, the AFM phase gives for states in the ground state, e.g., “bright green” and “dark green”, $\sigma_g \cdot \sigma_g = -1$. To obtain the phase boundary between AFM and FM CSL in terms of model parameters ϕ and θ [see Eq. (2)], we set their energies equal and obtain the condition

$$-\cos \phi + \sin \phi = -\frac{1}{3} \cos \phi + \frac{1}{9} \sin \phi, \quad (\text{C11})$$

which is independent of θ and therefore results in a straight line as seen in the phase diagram of Fig. 1(c). Solving Eq. (C11) results in

$$\frac{\phi}{\pi} = \frac{1}{\pi} \arctan\left(\frac{3}{4}\right) \approx 0.205. \quad (\text{C12})$$

In the AFM 3Q chiral ordered phase, the bond energy gives, e.g., for “bright green” and “dark blue”, $\sigma_g \cdot \sigma_b = 1/3$. We do the same comparison for the phase boundary between the FM CSL and the AFM 3Q chiral phases and obtain the condition

$$\cos \phi \sin \theta = -\cos \phi \sin \theta, \quad (\text{C13})$$

which is only fulfilled for

$$\cos \phi \sin \theta = 0. \quad (\text{C14})$$

Equation (C14) is satisfied for $\theta = 0$ or π , which corresponds to the pure Kitaev model, and for

$$\frac{\phi}{\pi} = \frac{1}{2}, \quad (\text{C15})$$

where the second solution $\phi/\pi = 3/2$ is physically irrelevant.

The phase boundaries described by Eqs. (C12) and (C15), are well visible in Fig. 1(c). The calculations for phase boundaries in the AFM CSL are straightforward, and give the symmetric solutions from the self-duality of $\mathcal{H}_{\text{BBQ-K}}^{8c}$, as written in Eq. (19).

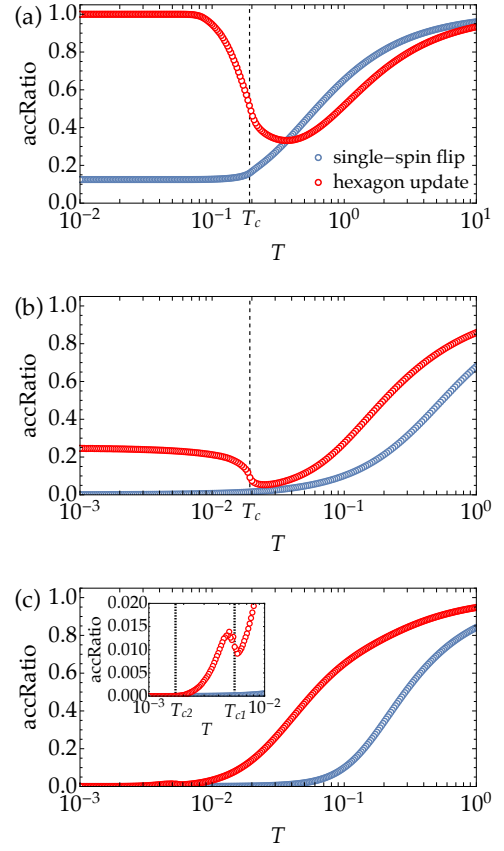


Figure 13. Temperature dependence of the acceptance ratio in the FM CSL as obtained in (a) the eight-color model, (b) the \mathbb{CP}^1 model, and (c) the \mathbb{CP}^2 model. Acceptance ratios for single-spin flip updates are depicted with blue circles, while results for hexagon updates are shown with red circles. Model parameters are the same as used in Figs. 4 (right column), 7, and 9. Simulations were performed for finite-size clusters of $L = 48$ ($N_S = 4608$).

Appendix D: Acceptance ratio for single-spin flip and hexagon cluster updates

Single-spin flip MC simulations within the CSL phase suffer from severe slowing down, making it impossible to decorrelate the MC samples using local spin updates. To overcome this issue, we combine single-spin flip updates with a hexagon cluster update as physically motivated from the nature of the eight-color CSL ground state manifold (see Fig. 3). Technical details of the implementation of the cluster update are given in Sec. IIIB 1 and Appendix A 2

In Figs. 13(a)–13(c) we show the temperature dependence of the acceptance ratio for single-spin flip and hexagon cluster updates in the eight-color model, the \mathbb{CP}^1 model, and the \mathbb{CP}^2 model, respectively. Model parameters are chosen to stabilize the FM CSL at low temperatures, as depicted in Figs. 4 (right column), 7, and 9. As expected from conventional MC simulations, the efficiency of the single-spin flip update monotonically decreases by reducing the temperature, showing a basically vanishing acceptance ratio below the transition into the CSL. We note that the value of $1/8$ in Fig. 13(a) comes

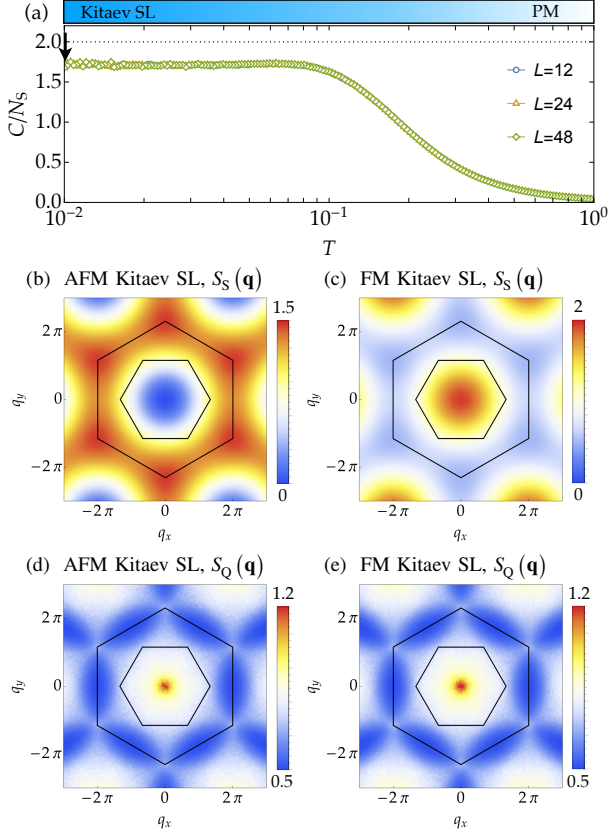


Figure 14. The semiclassical $S = 1$ Kitaev SL in the \mathbb{CP}^2 model, respectively at $\theta/\pi = 0$ and 1 of $\mathcal{H}_{\text{BBQ-K}}^A$ in Eq. (7). The specific heat C/N_S [Eq. (B1)] in (a) shows a crossover from a high-temperature paramagnet (PM) into the semiclassical analog of the Kitaev spin liquid (SL). The spin structure factors for dipoles, $S_S(\mathbf{q})$, and quadrupoles, $S_Q(\mathbf{q})$, [see Eqs. (B3)–(B5)] are shown respectively for the AFM Kitaev SL in (b) and (d), and for the FM Kitaev SL in (c) and (e). Simulations were performed at $T = 0.01$ [black arrow in (a)] for finite-size clusters of $L = 48$ ($N = 4608$).

from the fact that we accept a new state even when we sample over the same old state.

The hexagon update follows the same trend in the high-temperature regime. However, below the phase transition T_c in Figs. 13(a) and 13(b) and T_{c1} in Fig. 13(c), the acceptance ratio for the hexagon update increases and shows finite values. In fact, the hexagon update becomes rejection free in the eight-color model, while reaching up to $\approx 25\%$ in the \mathbb{CP}^1 model. The efficiency of the cluster update in the \mathbb{CP}^2 model is strongly suppressed ($\lesssim 1.5\%$), as shown in the inset of Fig. 13(c), but is still sufficient to decorrelate the finite-temperature FM CSL phase.

Appendix E: Additional dynamics simulations

In this Appendix we provide additional results of nontrivial dynamical structure factors for the semiclassical $S = 1$ AFM and FM Kitaev SL and the FM chiral spin liquid (CSL), as

discussed in Sec. III E,

1. Semiclassical dynamics of the $S = 1$ Kitaev spin liquid

In Fig. 14, we present thermodynamic properties of the semiclassical $S = 1$ AFM and FM Kitaev models at $\theta/\pi = 0$ and $\theta/\pi = 1$ of $\mathcal{H}_{\text{BBQ-K}}^A$ in Eq. (7). The specific heat C/N_S in Fig. 14(a) remains identical for AFM and FM Kitaev models, showing a crossover from a high-temperature paramagnet into a low-temperature cooperative paramagnet. Here, and throughout the main text, we refer to this cooperative paramagnetic phase as the semiclassical analog of the Kitaev SL. We numerically estimate a specific heat value in the limit of $T \rightarrow 0$, as

$$\frac{1}{N_S} C(T \rightarrow 0) = 1.712(2), \quad (\text{E1})$$

which is smaller than 2, providing direct evidence of zero-energy modes in the semiclassical ground state. The zero-energy modes are evident in the dynamical structure factors, as illustrated in Fig. 15.

We further present the equal-time structure factors of dipoles, $\tilde{S}_S(\mathbf{q})$, and quadrupoles, $\tilde{S}_Q(\mathbf{q})$, respectively for the AFM Kitaev SL in Figs. 14(b) and 14(d), and for the FM Kitaev SL in Figs. 14(c) and 14(e), at $T = 0.01$. The structure factors in both liquids are very diffuse and show in the dipole channel a strong similarity with the $S = 1/2$ Kitaev spin liquid [90, 138, 139]. Correlations for quadrupoles show quantitatively the same structure for both the AFM and the FM Kitaev SL states with high intensity at the Brillouin zone center and some weak structure reaching out to the Brillouin zone corners.

In Fig. 15, we present the dynamical structure factors [see Eqs. (B15)–(B17)] for the AFM and FM Kitaev SL phases at $T = 0.01$, for the same model parameters as used in Fig. 14. The structure factors for dipoles in Figs. 15(a) and 15(b) and their energy cross sections in Figs. 15(d)–15(g) show a strong resemblance to results for the $S = 1/2$ case [90], indicating that correlations are dominated by spin dipoles. Additionally, in Fig. 15(c), we show the quadrupole structure factor, which is equivalent between the AFM and FM Kitaev SL states, revealing a high-intensity zero-energy mode, consistently with the reduced specific heat value in Eq. (E1), and a flat band at $\omega/J \approx 2$. While the ground state is primarily dipolar, dipole characteristics implicitly influence the quadrupole components and lead to dominant zero-energy modes also in the $S_Q(\mathbf{q})$. The flat band, solely associated with quadrupole excitations, is determined by the interaction strength J_2 . Since $J_2 = 0$ in the “pure” Kitaev model, this quadrupole mode becomes dispersionless. The energy cross section in Fig. 15(h) captures the dominant quadrupole correlations at small ω , as it reproduces the pattern in the static structure factors of Figs. 14(d) and 14(e). A cross section through the flat band in Fig. 15(i) reveals a perfectly constant and featureless intensity, indicating the presence of localized excitations.

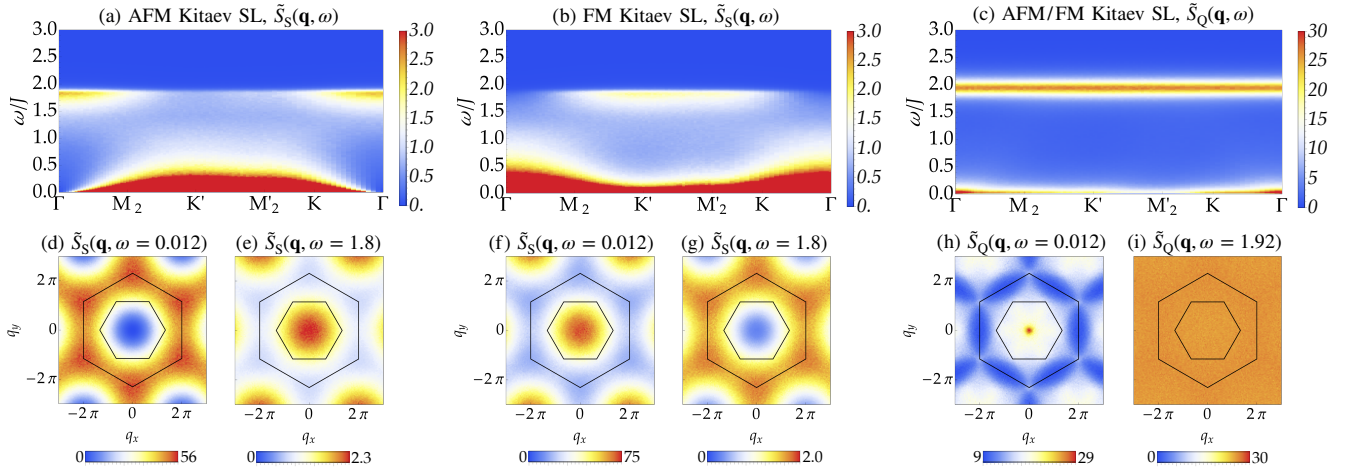


Figure 15. Dynamical structure factors [see Eqs. (B15)–(B17)] for the semiclassical analog of the $S = 1$ AFM and FM Kitaev SL in the \mathbb{CP}^2 model, respectively at $\theta/\pi = 0$ and 1 of $\mathcal{H}_{\text{BBQ-K}}^A$ in Eq. (7). (a) and (b) show dynamical structure factors of dipoles, $\tilde{S}_S(\mathbf{q}, \omega)$, respectively in the AFM and FM Kitaev SL states, with their energy cross sections in (d)–(g). Excitations are very similar to known results for the $S = 1/2$ Kitaev model, see Ref. [90]. (c) shows dynamical structure factors of quadrupoles, $\tilde{S}_Q(\mathbf{q}, \omega)$, with energy cross sections in (h)–(i). The signals for AFM and FM Kitaev SL are equivalent [see Fig. 14(d) and 14(e)], and therefore shown only once. Data were obtained from molecular dynamics simulations (details in Appendix A3) for finite-size clusters of $L = 48$ ($N = 4608$), at temperatures $T = 0.01$ [black arrow in Fig. 14(a)]. (a)–(c) are plotted along the green path in momentum space, as indicated in the left panel of Fig. 9(d).

2. Dynamics of the FM CSL – comparison between \mathbb{CP}^2 and \mathbb{CP}^1 models

The eight-color model describes a system where the spin degree of freedom is discretized, and consequently lacks dynamics. Fortunately, as discussed in Secs. III C and III D, the CSL is stabilized in models with continuous spin degree of freedom, which allows us to simulate its dynamical properties (see technical details in Appendix A3). Here, we compare the dynamical structure factors of the FM CSL between the \mathbb{CP}^2 model and the \mathbb{CP}^1 model, and demonstrate that their qualitative signatures are essentially the same.

In Fig. 16, we show the dynamical structure factors for spin-dipole moments, $\tilde{S}_S(\mathbf{q}, \omega)$ [see Eqs. (B15) and (B17)], in the FM CSL phase for both the \mathbb{CP}^2 model and the \mathbb{CP}^1 model, at the same model parameters of $\theta/\pi = 0.06$ and $\phi/\pi = 0.305$. The top row shows the spectrum along the path in momentum space as indicated by green lines in the left panel of Fig. 9(d). The bottom row depicts frequency cuts at the explicit momentum points Γ and K' .

For better comparison we replot in Fig. 16(a) the result from the \mathbb{CP}^2 model, as previously shown in Fig. 10(b). The spectrum exhibits three energy regimes: a zero-energy flat band, a slightly gapped diffuse band, and a largely gapped and diffuse continuum with broad bandwidth at higher energies. Additionally, a flat, weak intensity band around $\omega/J \approx 2$ is observed, arising from the mixing between dipole and quadrupole excitations due to spin anisotropy. These energy

regimes are quantified in the bottom row.

In Fig. 16(b), qualitatively similar features are visible in the dispersion obtained from \mathbb{CP}^1 model simulations, performed at nearly the same temperature. Here, the diffuse band at intermediate energies exhibits a larger bandwidth while clearly showing an energy gap to the high-intensity zero-energy mode. The broad continuum is slightly shifted to higher energies compared to the \mathbb{CP}^2 case but demonstrates almost the same intensity distribution. The nearly flat band around $\omega/J \approx 2$ is absent in the \mathbb{CP}^1 case, as quadrupoles are strictly excluded in these simulations.

In Fig. 16(c), we additionally present the spectrum for the \mathbb{CP}^1 model at $T = 0.001$, a temperature that is not accessible in the \mathbb{CP}^2 model, as the FM CSL transitions into the NC-1 ordered state before reaching such low temperatures (see thermodynamics in Sec. III D 2). Since thermal fluctuations are reduced, the spectrum becomes slightly sharper, especially the gap of the diffuse intermediate band to the zero-energy mode becomes more pronounced. However, importantly, qualitative features between \mathbb{CP}^1 and \mathbb{CP}^2 model simulations remain the same.

This comparison confirms our intuition that dominant properties of the CSL are still captured in the \mathbb{CP}^1 model, which includes only dipole spin degree of freedom. Additionally, simulation results for the dynamics in both the \mathbb{CP}^1 and \mathbb{CP}^2 models reveal a very diffuse and gapped continuum, associated with the excitations of the FM CSL, as discussed in the eight-color model in Sec. III B.

[1] G. Chen, R. Pereira, and L. Balents, *Exotic phases induced by strong spin-orbit coupling in ordered double perovskites*,

Phys. Rev. B **82**, 174440 (2010).

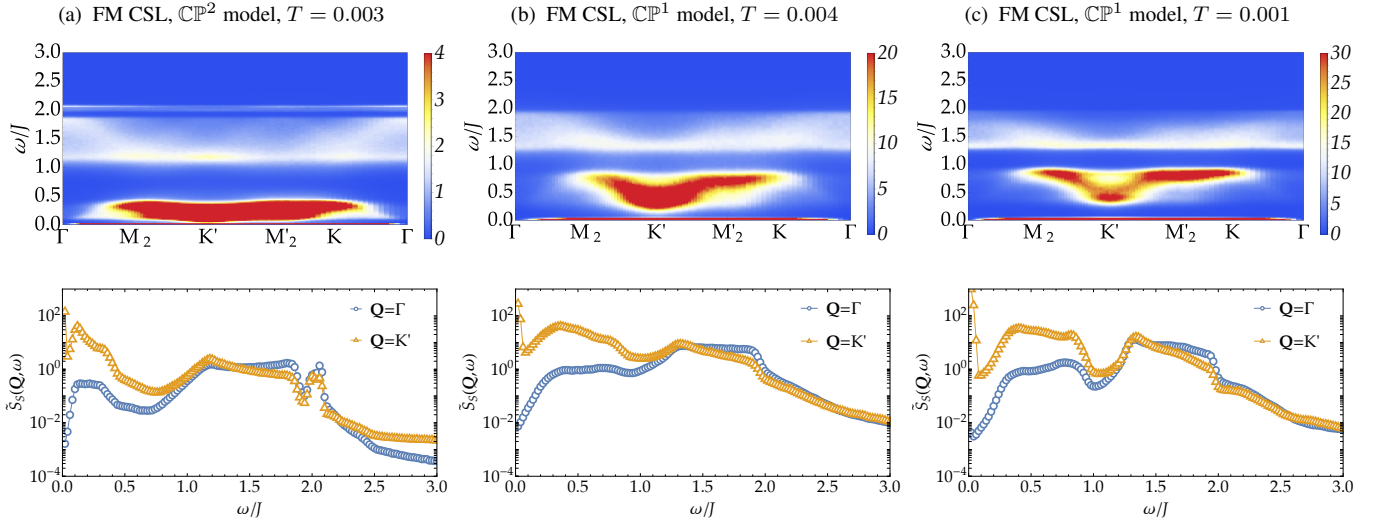


Figure 16. Dynamical structure factors for spin-dipole moments, $\tilde{S}_S(\mathbf{q}, \omega)$ [see Eq. (B17)], in the FM CSL phase. Results in the top row are shown along the path indicated by green lines in the left panel of Fig. 9(d), while the bottom row shows frequency-line cuts at the Γ and K' momentum points. All results are presented for the same model parameters: $\theta/\pi = 0.06$ and $\phi/\pi = 0.305$ [see Eq. (2)], and are compared between \mathbb{CP}^2 model [Eqs. (7) and (A8)] and \mathbb{CP}^1 model [Eqs. (1) and (A13)] calculations. (a) Results for the \mathbb{CP}^2 model at $T = 0.003$ [c.f. Fig. 10(b)]. (b) Results for the \mathbb{CP}^1 model at a comparable temperature, $T = 0.004$, exhibiting essentially the same features as observed for the \mathbb{CP}^2 model in (a). (c) Results in the \mathbb{CP}^1 model at very low temperatures, $T = 0.001$. Data were obtained from molecular dynamics simulations (details in Appendix A 3) for finite-size clusters of $L = 48$ ($N = 4608$).

- [2] L. Fu, *Parity-Breaking Phases of Spin-Orbit-Coupled Metals with Gyrotropic, Ferroelectric, and Multipolar Orders*, *Phys. Rev. Lett.* **115**, 026401 (2015).
- [3] D. Hirai, H. Sagayama, S. Gao, H. Ohsumi, G. Chen, T.-h. Arima, and Z. Hiroi, *Detection of multipolar orders in the spin-orbit-coupled 5d Mott insulator $\text{Ba}_2\text{MgReO}_6$* , *Phys. Rev. Res.* **2**, 022063 (2020).
- [4] D. D. Maharaj, G. Sala, M. B. Stone, E. Kermarrec, C. Ritter, F. Fauth, C. A. Marjerrison, J. E. Greedan, A. Paramakanti, and B. D. Gaulin, *Octupolar versus Néel Order in Cubic 5d² Double Perovskites*, *Phys. Rev. Lett.* **124**, 087206 (2020).
- [5] A. Paramakanti, D. D. Maharaj, and B. D. Gaulin, *Octupolar order in d-orbital Mott insulators*, *Phys. Rev. B* **101**, 054439 (2020).
- [6] P. Thalmeier, T. Takimoto, J. Chang, and I. Eremin, *Multipolar Order and Superconductivity in f-Electron Compounds*, *Journal of the Physical Society of Japan* **77**, 43 (2008).
- [7] K. Matsubayashi, T. Tanaka, A. Sakai, S. Nakatsuji, Y. Kubo, and Y. Uwatoko, *Pressure-Induced Heavy Fermion Superconductivity in the Nonmagnetic Quadrupolar System $\text{PrTi}_2\text{Al}_{20}$* , *Phys. Rev. Lett.* **109**, 187004 (2012).
- [8] F. Freyer, J. Attig, S. Lee, A. Paramakanti, S. Trebst, and Y. B. Kim, *Two-stage multipolar ordering in $\text{PrTi}_2\text{Al}_{20}$ Kondo materials*, *Phys. Rev. B* **97**, 115111 (2018).
- [9] S. Lee, S. Trebst, Y. B. Kim, and A. Paramakanti, *Landau theory of multipolar orders in $\text{Pr}(Y)_2X_{20}$ Kondo materials ($Y = \text{Ti, V, Rh, Ir}$; $X = \text{Al, Zn}$)*, *Phys. Rev. B* **98**, 134447 (2018).
- [10] G. Sim, A. Mishra, M. J. Park, Y. B. Kim, G. Y. Cho, and S. Lee, *Multipolar superconductivity in Luttinger semimetals*, *Phys. Rev. Res.* **2**, 023416 (2020).
- [11] A. S. Patri and Y. B. Kim, *Unconventional Superconductivity arising from Multipolar Kondo Interactions*, *SciPost Phys.* **12**, 057 (2022).
- [12] Wladimir A. Benalcazar and B. Andrei Bernevig and Taylor L. Hughes, *Quantized electric multipole insulators*, *Science* **357**, 61 (2017).
- [13] J. Romhányi, *Multipolar edge states in the anisotropic kagome antiferromagnet*, *Phys. Rev. B* **99**, 014408 (2019).
- [14] R. Sibille, E. Lhotel, V. Pomjakushin, C. Baines, T. Fennell, and M. Kenzelmann, *Candidate Quantum Spin Liquid in the Ce^{3+} Pyrochlore Stannate $\text{Ce}_2\text{Sn}_2\text{O}_7$* , *Phys. Rev. Lett.* **115**, 097202 (2015).
- [15] J. Gaudet, E. M. Smith, J. Dudemaine, J. Beare, C. R. C. Buhariwalla, N. P. Butch, M. B. Stone, A. I. Kolesnikov, G. Xu, D. R. Yahne, K. A. Ross, C. A. Marjerrison, J. D. Garrett, G. M. Luke, A. D. Bianchi, and B. D. Gaulin, *Quantum Spin Ice Dynamics in the Dipole-Octupole Pyrochlore Magnet $\text{Ce}_2\text{Zr}_2\text{O}_7$* , *Phys. Rev. Lett.* **122**, 187201 (2019).
- [16] R. Sibille, N. Gauthier, E. Lhotel, V. Porée, V. Pomjakushin, R. A. Ewings, T. G. Perring, J. Ollivier, A. Wildes, C. Ritter, T. C. Hansen, D. A. Keen, G. J. Nilsen, L. Keller, S. Petit, and T. Fennell, *A quantum liquid of magnetic octupoles on the pyrochlore lattice*, *Nature Physics* **16**, 546 (2020).
- [17] Y. Akagi, Y. Amari, N. Sawado, and Y. Shnir, *Isolated skyrmions in the \mathbb{CP}^2 nonlinear sigma model with a Dzyaloshinskii-Moriya type interaction*, *Phys. Rev. D* **103**, 065008 (2021).
- [18] Y. Amari, Y. Akagi, S. B. Gudnason, M. Nitta, and Y. Shnir, *\mathbb{CP}^2 skyrmion crystals in an $SU(3)$ magnet with a generalized Dzyaloshinskii-Moriya interaction*, *Phys. Rev. B* **106**, L100406 (2022).
- [19] H. Zhang, Z. Wang, D. Dahlbom, K. Barros, and C. D. Batista, *\mathbb{CP}^2 skyrmions and skyrmion crystals in realistic quantum magnets*, *Nature Communications* **14**, 3626 (2023).
- [20] H.-H. Lai, E. M. Nica, W.-J. Hu, S.-S. Gong, S. Paschen, and Q. Si, *Kondo Destruction and Multipolar Order—Implications for Heavy Fermion Quantum Criticality* (2018),

- arXiv:1807.09258 [cond-mat.str-el].
- [21] R. Masui and K. Totsuka, *Electric and magnetic properties of higher-spin Kondo-Heisenberg models at strong coupling*, *Phys. Rev. B* **106**, 014411 (2022).
 - [22] N. Papanicolaou, *Unusual phases in quantum spin-1 systems*, *Nuclear Physics B* **305**, 367 (1988).
 - [23] H. Tsunetsugu and M. Arikawa, *Spin Nematic Phase in $S=1$ Triangular Antiferromagnets*, *Journal of the Physical Society of Japan* **75**, 083701 (2006).
 - [24] A. Läuchli, F. Mila, and K. Penc, *Quadrupolar Phases of the $S = 1$ Bilinear-Biquadratic Heisenberg Model on the Triangular Lattice*, *Phys. Rev. Lett.* **97**, 087205 (2006).
 - [25] K. Penc and A. M. Läuchli, *Spin Nematic Phases in Quantum Spin Systems*, in *Introduction to Frustrated Magnetism: Materials, Experiments, Theory*, edited by C. Lacroix, P. Mendels, and F. Mila (Springer Berlin Heidelberg, Berlin, Heidelberg, 2011) pp. 331–362.
 - [26] H. Kelker, *History of Liquid Crystals*, *Molecular Crystals and Liquid Crystals* **21**, 1 (1973).
 - [27] H. Kelker, *Survey of the Early History of Liquid Crystals*, *Molecular Crystals and Liquid Crystals Incorporating Nonlinear Optics* **165**, 1 (1988).
 - [28] P. de Gennes and J. Prost, *The Physics of Liquid Crystals*, International Series of Monographs on Physics (Clarendon Press, 1993).
 - [29] N. D. Mermin and H. Wagner, *Absence of Ferromagnetism or Antiferromagnetism in One- or Two-Dimensional Isotropic Heisenberg Models*, *Phys. Rev. Lett.* **17**, 1133 (1966).
 - [30] G. P. Alexander, B. G.-g. Chen, E. A. Matsumoto, and R. D. Kamien, *Colloquium: Disclination loops, point defects, and all that in nematic liquid crystals*, *Rev. Mod. Phys.* **84**, 497 (2012).
 - [31] I. Chuang, R. Durrer, N. Turok, and B. Yurke, *Cosmology in the Laboratory: Defect Dynamics in Liquid Crystals*, *Science* **251**, 1336 (1991).
 - [32] M. J. Bowick, L. Chandar, E. A. Schiff, and A. M. Srivastava, *The Cosmological Kibble Mechanism in the Laboratory: String Formation in Liquid Crystals*, *Science* **263**, 943 (1994).
 - [33] G. Volovik, *Superfluid $^3\text{He-B}$ and gravity*, *Physica B: Condensed Matter* **162**, 222 (1990).
 - [34] G. E. Volovik, *The universe in a helium droplet*, Repr ed., International series of monographs on physics No. 117 (Oxford University Press, Oxford, 2009).
 - [35] L. Chojnacki, R. Pohle, H. Yan, Y. Akagi, and N. Shannon, *Gravitational wave analogues in spin nematics and cold atoms* (2023), arXiv:2310.10078 [cond-mat.str-el].
 - [36] M. Blume and Y. Y. Hsieh, *Biquadratic Exchange and Quadrupolar Ordering*, *Journal of Applied Physics* **40**, 1249 (1969).
 - [37] V. M. Matveev, *Quantum quadrupolar magnetism and phase transitions in the presence of biquadratic exchange*, *JETP* **38**, 813 (1974).
 - [38] A. F. Andreev and I. A. Grishchuk, *Spin nematics*, *JETP* **60**, 267 (1984).
 - [39] A. Smerald and N. Shannon, *Theory of spin excitations in a quantum spin-nematic state*, *Phys. Rev. B* **88**, 184430 (2013).
 - [40] F. Michaud, F. Vernay, and F. Mila, *Theory of inelastic light scattering in spin-1 systems: Resonant regimes and detection of quadrupolar order*, *Phys. Rev. B* **84**, 184424 (2011).
 - [41] M. E. Valentine, T. Higo, Y. Nambu, D. Chaudhuri, J. Wen, C. Broholm, S. Nakatsuji, and N. Drichko, *Impact of the Lattice on Magnetic Properties and Possible Spin Nematicity in the $S = 1$ Triangular Antiferromagnet NiGa_2S_4* , *Phys. Rev. Lett.* **125**, 197201 (2020).
 - [42] L. Savary and T. Senthil, *Probing Hidden Orders with Resonant Inelastic X-Ray Scattering* (2015), arXiv:1506.04752 [cond-mat.str-el].
 - [43] H. Takahashi, H. Suzuki, J. Bertinshaw, S. Bette, C. Mühle, J. Nuss, R. Dinnebier, A. Yaresko, G. Khaliullin, H. Gretarsson, T. Takayama, H. Takagi, and B. Keimer, *Nonmagnetic $J = 0$ State and Spin-Orbit Excitations in K_2RuCl_6* , *Phys. Rev. Lett.* **127**, 227201 (2021).
 - [44] A. Nag, A. Nocera, S. Agrestini, M. Garcia-Fernandez, A. C. Walters, S.-W. Cheong, S. Johnston, and K.-J. Zhou, *Quadrupolar magnetic excitations in an isotropic spin-1 antiferromagnet*, *Nature Communications* **13**, 2327 (2022).
 - [45] Y. Kohama, H. Ishikawa, A. Matsuo, K. Kindo, N. Shannon, and Z. Hiroi, *Possible observation of quantum spin-nematic phase in a frustrated magnet*, *Proceedings of the National Academy of Sciences* **116**, 10686 (2019).
 - [46] H. Zhang and C. D. Batista, *Classical spin dynamics based on $\text{SU}(N)$ coherent states*, *Phys. Rev. B* **104**, 104409 (2021).
 - [47] K. Remund, R. Pohle, Y. Akagi, J. Romhányi, and N. Shannon, *Semi-classical simulation of spin-1 magnets*, *Phys. Rev. Research* **4**, 033106 (2022).
 - [48] D. Dahlbom, H. Zhang, C. Miles, X. Bai, C. D. Batista, and K. Barros, *Geometric integration of classical spin dynamics via a mean-field Schrödinger equation*, *Phys. Rev. B* **106**, 054423 (2022).
 - [49] D. Dahlbom, C. Miles, H. Zhang, C. D. Batista, and K. Barros, *Langevin dynamics of generalized spins as $\text{SU}(N)$ coherent states*, *Phys. Rev. B* **106**, 235154 (2022).
 - [50] R. Iwazaki, H. Shinaoka, and S. Hoshino, *Material-based analysis of spin-orbital Mott insulators*, *Phys. Rev. B* **108**, L241108 (2023).
 - [51] <https://github.com/SunnySuite/Sunny.jl>.
 - [52] S. Nakatsuji, Y. Nambu, H. Tonomura, O. Sakai, S. Jonas, C. Broholm, H. Tsunetsugu, Y. Qiu, and Y. Maeno, *Spin Disorder on a Triangular Lattice*, *Science* **309**, 1697 (2005), <https://www.science.org/doi/pdf/10.1126/science.1114727>.
 - [53] E. M. Stoudenmire, S. Trebst, and L. Balents, *Quadrupolar correlations and spin freezing in $S = 1$ triangular lattice antiferromagnets*, *Phys. Rev. B* **79**, 214436 (2009).
 - [54] X. Bai, S.-S. Zhang, Z. Dun, H. Zhang, Q. Huang, H. Zhou, M. B. Stone, A. I. Kolesnikov, F. Ye, C. D. Batista, and M. Mourigal, *Hybridized quadrupolar excitations in the spin-anisotropic frustrated magnet FeI_2* , *Nature Physics* **17**, 467 (2021).
 - [55] D. Dahlbom, F. T. Brooks, M. S. Wilson, S. Chi, A. I. Kolesnikov, M. B. Stone, H. Cao, Y.-W. Li, K. Barros, M. Mourigal, C. D. Batista, and X. Bai, *Quantum-to-classical crossover in generalized spin systems: Temperature-dependent spin dynamics of FeI_2* , *Phys. Rev. B* **109**, 014427 (2024).
 - [56] S.-H. Do, H. Zhang, D. A. Dahlbom, T. J. Williams, V. O. Garlea, T. Hong, T.-H. Jang, S.-W. Cheong, J.-H. Park, K. Barros, C. D. Batista, and A. D. Christianson, *Understanding temperature-dependent $\text{SU}(3)$ spin dynamics in the $S = 1$ antiferromagnet $\text{Ba}_2\text{FeSi}_2\text{O}_7$* , *npj Quantum Materials* **8**, 5 (2023).
 - [57] G. Baskaran, D. Sen, and R. Shankar, *Spin- S Kitaev model: Classical ground states, order from disorder, and exact correlation functions*, *Phys. Rev. B* **78**, 115116 (2008).
 - [58] A. Koga, H. Tomishige, and J. Nasu, *Ground-state and Thermodynamic Properties of an $S = 1$ Kitaev Model*, *Journal of the Physical Society of Japan* **87**, 063703 (2018).
 - [59] T. Suzuki and Y. Yamaji, *Thermal properties of spin- S Kitaev-Heisenberg model on a honeycomb lattice*, *Physica B: Con-*

- densed Matter **536**, 637 (2018).
- [60] J. Oitmaa, A. Koga, and R. R. P. Singh, *Incipient and well-developed entropy plateaus in spin- S Kitaev models*, *Phys. Rev. B* **98**, 214404 (2018).
- [61] X.-Y. Dong and D. N. Sheng, *Spin-1 Kitaev-Heisenberg model on a honeycomb lattice*, *Phys. Rev. B* **102**, 121102 (2020).
- [62] C. Hickey, C. Berke, P. P. Stavropoulos, H.-Y. Kee, and S. Trebst, *Field-driven gapless spin liquid in the spin-1 Kitaev honeycomb model*, *Phys. Rev. Res.* **2**, 023361 (2020).
- [63] H.-Y. Lee, N. Kawashima, and Y. B. Kim, *Tensor network wave function of $S = 1$ Kitaev spin liquids*, *Phys. Rev. Res.* **2**, 033318 (2020).
- [64] I. Khait, P. P. Stavropoulos, H.-Y. Kee, and Y. B. Kim, *Characterizing spin-one Kitaev quantum spin liquids*, *Phys. Rev. Res.* **3**, 013160 (2021).
- [65] K. Fukui, Y. Kato, J. Nasu, and Y. Motome, *Ground-state phase diagram of spin- S Kitaev-Heisenberg models*, *Phys. Rev. B* **106**, 174416 (2022).
- [66] A. Rayyan, D. Churchill, and H.-Y. Kee, *Field-induced Kitaev multipolar liquid in spin-orbit coupled d^2 honeycomb Mott insulators*, *Phys. Rev. B* **107**, L020408 (2023).
- [67] H. Ma, *\mathbb{Z}_2 Spin Liquids in the Higher Spin- S Kitaev Honeycomb Model: An Exact Deconfined \mathbb{Z}_2 Gauge Structure in a Nonintegrable Model*, *Phys. Rev. Lett.* **130**, 156701 (2023).
- [68] R. Liu, H. T. Lam, H. Ma, and L. Zou, *Symmetries and anomalies of Kitaev spin- S models: Identifying symmetry-enforced exotic quantum matter*, *SciPost Phys.* **16**, 100 (2024).
- [69] M. Georgiou, I. Rousochatzakis, D. J. J. Farnell, J. Richter, and R. F. Bishop, *Spin- S Kitaev-Heisenberg model on the honeycomb lattice: A high-order treatment via the many-body coupled cluster method* (2024), [arXiv:2405.14378 \[cond-mat.str-el\]](https://arxiv.org/abs/2405.14378).
- [70] H.-K. Jin, W. M. H. Natori, F. Pollmann, and J. Knolle, *Unveiling the $S=3/2$ Kitaev honeycomb spin liquids*, *Nature Communications* **13**, 3813 (2022).
- [71] V. S. de Carvalho, H. Freire, and R. G. Pereira, *Multipolar spin liquid in an exactly solvable model for $j_{\text{eff}} = \frac{3}{2}$ moments*, *Phys. Rev. B* **108**, 094418 (2023).
- [72] P. P. Stavropoulos, D. Pereira, and H.-Y. Kee, *Microscopic Mechanism for a Higher-Spin Kitaev Model*, *Phys. Rev. Lett.* **123**, 037203 (2019).
- [73] A. Scheie, K. Ross, P. P. Stavropoulos, E. Seibel, J. A. Rodriguez-Rivera, J. A. Tang, Y. Li, H.-Y. Kee, R. J. Cava, and C. Broholm, *Counterrotating magnetic order in the honeycomb layers of $\text{NaNi}_2\text{BiO}_{6-\delta}$* , *Phys. Rev. B* **100**, 214421 (2019).
- [74] K. M. Taddei, V. O. Garlea, A. M. Samarakoon, L. D. Sanjeeva, J. Xing, T. W. Heitmann, C. dela Cruz, A. S. Sefat, and D. Parker, *Zigzag magnetic order and possible Kitaev interactions in the spin-1 honeycomb lattice KNiAsO_4* , *Phys. Rev. Res.* **5**, 013022 (2023).
- [75] R. Pohle, N. Shannon, and Y. Motome, *Spin nematics meet spin liquids: Exotic quantum phases in the spin-1 bilinear-biquadratic model with Kitaev interactions*, *Phys. Rev. B* **107**, L140403 (2023).
- [76] A. Kitaev, *Anyons in an exactly solved model and beyond*, *Annals of Physics* **321**, 2 (2006), January Special Issue.
- [77] A. M. Perelomov, *Coherent states for arbitrary Lie group*, *Communications in Mathematical Physics* **26**, 222 (1972).
- [78] S. Gnutzmann and M. Kus, *Coherent states and the classical limit on irreducible representations*, *Journal of Physics A: Mathematical and General* **31**, 9871 (1998).
- [79] K. Nemoto, *Generalized coherent states for $SU(n)$ systems*, *Journal of Physics A: Mathematical and General* **33**, 3493 (2000).
- [80] J. Bradbury, R. Frostig, P. Hawkins, M. J. Johnson, C. Leary, D. Maclaurin, G. Necula, A. Paszke, J. VanderPlas, S. Wanderman-Milne, and Q. Zhang, *JAX: composable transformations of Python+NumPy programs* (2018).
- [81] I. Babuschkin, K. Baumli, A. Bell, S. Bhupatiraju, J. Bruce, P. Buchlovsky, D. Budden, T. Cai, A. Clark, I. Danihelka, C. Fantacci, J. Godwin, C. Jones, R. Hemsley, T. Hennigan, M. Hessel, S. Hou, S. Kapturowski, T. Keck, I. Kemaev, M. King, M. Kunesch, L. Martens, H. Merzic, V. Mikulik, T. Norman, J. Quan, G. Papamakarios, R. Ring, F. Ruiz, A. Sanchez, R. Schneider, E. Sezener, S. Spencer, S. Srinivasan, L. Wang, W. Stokowiec, and F. Viola, *The DeepMind JAX Ecosystem* (2020).
- [82] H. H. Zhao, C. Xu, Q. N. Chen, Z. C. Wei, M. P. Qin, G. M. Zhang, and T. Xiang, *Plaquette order and deconfined quantum critical point in the spin-1 bilinear-biquadratic Heisenberg model on the honeycomb lattice*, *Phys. Rev. B* **85**, 134416 (2012).
- [83] I. Martin and C. D. Batista, *Itinerant Electron-Driven Chiral Magnetic Ordering and Spontaneous Quantum Hall Effect in Triangular Lattice Models*, *Phys. Rev. Lett.* **101**, 156402 (2008).
- [84] Y. Akagi and Y. Motome, *Spin Chirality Ordering and Anomalous Hall Effect in the Ferromagnetic Kondo Lattice Model on a Triangular Lattice*, *Journal of the Physical Society of Japan* **79**, 083711 (2010).
- [85] L. Messio, C. Lhuillier, and G. Misguich, *Lattice symmetries and regular magnetic orders in classical frustrated antiferromagnets*, *Phys. Rev. B* **83**, 184401 (2011).
- [86] I. Niesen and P. Corboz, *A tensor network study of the complete ground state phase diagram of the spin-1 bilinear-biquadratic Heisenberg model on the square lattice*, *SciPost Phys.* **3**, 030 (2017).
- [87] We notice several complicated phases around the two $SU(3)$ points at $(\theta/\pi, \phi/\pi) = (0.5, 0.25)$ and $(0.5, 0.5)$, which will be discussed elsewhere.
- [88] P. Corboz, M. Lajkó, K. Penc, F. Mila, and A. M. Läuchli, *Competing states in the $SU(3)$ Heisenberg model on the honeycomb lattice: Plaquette valence-bond crystal versus dimerized color-ordered state*, *Phys. Rev. B* **87**, 195113 (2013).
- [89] Values in parentheses represent the statistical error in the last digit, determined by the standard deviation among five independent simulation runs.
- [90] A. M. Samarakoon, A. Banerjee, S.-S. Zhang, Y. Kamiya, S. E. Nagler, D. A. Tennant, S.-H. Lee, and C. D. Batista, *Comprehensive study of the dynamics of a classical Kitaev spin liquid*, *Phys. Rev. B* **96**, 134408 (2017).
- [91] We observed several unconventional phases near the two $SU(3)$ points at $(\theta/\pi, \phi/\pi) = (0.5, 0.25)$ and $(0.5, 0.5)$, which we reserve for a more in-depth discussion in the future.
- [92] V. Kalmeyer and R. B. Laughlin, *Equivalence of the resonating-valence-bond and fractional quantum Hall states*, *Phys. Rev. Lett.* **59**, 2095 (1987).
- [93] X. G. Wen, F. Wilczek, and A. Zee, *Chiral spin states and superconductivity*, *Phys. Rev. B* **39**, 11413 (1989).
- [94] D. F. Schroeter, E. Kapit, R. Thomale, and M. Greiter, *Spin Hamiltonian for which the Chiral Spin Liquid is the Exact Ground State*, *Phys. Rev. Lett.* **99**, 097202 (2007).
- [95] H. Yao and S. A. Kivelson, *Exact Chiral Spin Liquid with Non-Abelian Anyons*, *Phys. Rev. Lett.* **99**, 247203 (2007).
- [96] J. Fu, *Exact chiral-spin-liquid state in a Kitaev-type spin model*, *Phys. Rev. B* **100**, 195131 (2019).
- [97] V. Peri, S. Ok, S. S. Tsirkin, T. Neupert, G. Baskaran, M. Gre-

- iter, R. Moessner, and R. Thomale, *Non-Abelian chiral spin liquid on a simple non-Archimedean lattice*, *Phys. Rev. B* **101**, 041114 (2020).
- [98] T. Momoi, K. Kubo, and K. Niki, *Possible Chiral Phase Transition in Two-Dimensional Solid ^3He* , *Phys. Rev. Lett.* **79**, 2081 (1997).
- [99] Y. Kato, I. Martin, and C. D. Batista, *Stability of the Spontaneous Quantum Hall State in the Triangular Kondo-Lattice Model*, *Phys. Rev. Lett.* **105**, 266405 (2010).
- [100] J. Nasu and Y. Motome, *Thermodynamics of Chiral Spin Liquids with Abelian and Non-Abelian Anyons*, *Phys. Rev. Lett.* **115**, 087203 (2015).
- [101] Y. Kato, Y. Kamiya, J. Nasu, and Y. Motome, *Chiral spin liquids at finite temperature in a three-dimensional Kitaev model*, *Phys. Rev. B* **96**, 174409 (2017).
- [102] P. A. Mishchenko, Y. Kato, K. O'Brien, T. A. Bojesen, T. Eschmann, M. Hermanns, S. Trebst, and Y. Motome, *Chiral spin liquids with crystalline \mathbb{Z}_2 gauge order in a three-dimensional Kitaev model*, *Phys. Rev. B* **101**, 045118 (2020).
- [103] D. Lozano-Gómez, Y. Iqbal, and M. Vojta, *A Classical Chiral Spin-Liquid from Chiral Interactions on the Pyrochlore Lattice* (2024), [arXiv:2403.10601 \[cond-mat.str-el\]](#).
- [104] H. Yan and R. Pohle, in preparation.
- [105] Z. Nussinov and J. van den Brink, *Compass models: Theory and physical motivations*, *Rev. Mod. Phys.* **87**, 1 (2015).
- [106] D. Dahlbom, H. Zhang, Z. Laraib, D. M. Pajerowski, K. Barros, and C. Batista, *Renormalized Classical Theory of Quantum Magnets* (2023), [arXiv:2304.03874 \[cond-mat.str-el\]](#).
- [107] H. Kawamura and A. Yamamoto, *Vortex-Induced Topological Transition of the Bilinear-Biquadratic Heisenberg Antiferromagnet on the Triangular Lattice*, *Journal of the Physical Society of Japan* **76**, 073704 (2007).
- [108] S. E. Korshunov, F. Mila, and K. Penc, *Degeneracy and ordering of the noncoplanar phase of the classical bilinear-biquadratic Heisenberg model on the triangular lattice*, *Phys. Rev. B* **85**, 174420 (2012).
- [109] P. Mellado, *Spin model for the honeycomb NiPS_3* , *Applied Physics Letters* **123**, 242403 (2023).
- [110] T. Mashiko and T. Okubo, *Quantum phase transition between spin liquid and spin nematics in spin-1 Kitaev honeycomb model* (2024), [arXiv:2403.11490 \[cond-mat.stat-mech\]](#).
- [111] Q. Luo, J. Zhao, J. Li, and X. Wang, *Chiral spin state and nematic ferromagnet in the spin-1 Kitaev- Γ model* (2024), [arXiv:2403.08382 \[cond-mat.str-el\]](#).
- [112] A. Singhanian, J. van den Brink, and S. Nishimoto, *Emergence of vortex state in the $S = 1$ Kitaev-Heisenberg model with single-ion anisotropy* (2023), [arXiv:2311.14161 \[cond-mat.str-el\]](#).
- [113] A. Ralko and J. Merino, *Chiral bosonic quantum spin liquid in the integer-spin Heisenberg-Kitaev model* (2024), [arXiv:2405.10731 \[cond-mat.str-el\]](#).
- [114] A. Läuchli, G. Schmid, and S. Trebst, *Spin nematics correlations in bilinear-biquadratic $S = 1$ spin chains*, *Phys. Rev. B* **74**, 144426 (2006).
- [115] L. Savary, *Quantum loop states in spin-orbital models on the honeycomb lattice*, *Nature Communications* **12**, 3004 (2021).
- [116] M. Gohlke, J. C. Pelayo, and T. Suzuki, *Extended Quantum Spin Liquid with Spinon-like Excitations in an Anisotropic Kitaev-Gamma Model* (2022), [arXiv:2212.11000 \[cond-mat.str-el\]](#).
- [117] S. Feng, A. Agarwala, and N. Trivedi, *Dimensional reduction of Kitaev spin liquid at quantum criticality*, *Phys. Rev. Res.* **6**, 013298 (2024).
- [118] O. Tchernyshyov and G.-W. Chern, *Spin-Lattice Coupling in Frustrated Antiferromagnets*, in *Introduction to Frustrated Magnetism: Materials, Experiments, Theory*, edited by C. Lacroix, P. Mendels, and F. Mila (Springer Berlin Heidelberg, Berlin, Heidelberg, 2011) pp. 269–291.
- [119] A. Yoshimori and S. Inagaki, *Fourth Order Interaction Effects on the Antiferromagnetic Structures. II. A Phenomenological Model for NiS_2* , *Journal of the Physical Society of Japan* **50**, 769 (1981).
- [120] M. Hoffmann and S. Blügel, *Systematic derivation of realistic spin models for beyond-Heisenberg solids*, *Phys. Rev. B* **101**, 024418 (2020).
- [121] R. Soni, N. Kaushal, C. Şen, F. A. Reboredo, A. Moreo, and E. Dagotto, *Estimation of biquadratic and bicubic Heisenberg effective couplings from multiorbital Hubbard models*, *New Journal of Physics* **24**, 073014 (2022).
- [122] H. Katsura, N. Nagaosa, and P. A. Lee, *Theory of the Thermal Hall Effect in Quantum Magnets*, *Phys. Rev. Lett.* **104**, 066403 (2010).
- [123] Y. Onose, T. Ideue, H. Katsura, Y. Shiomi, N. Nagaosa, and Y. Tokura, *Observation of the Magnon Hall Effect*, *Science* **329**, 297 (2010).
- [124] R. Matsumoto and S. Murakami, *Theoretical Prediction of a Rotating Magnon Wave Packet in Ferromagnets*, *Phys. Rev. Lett.* **106**, 197202 (2011).
- [125] L. Janssen, E. C. Andrade, and M. Vojta, *Honeycomb-Lattice Heisenberg-Kitaev Model in a Magnetic Field: Spin Canting, Metamagnetism, and Vortex Crystals*, *Phys. Rev. Lett.* **117**, 277202 (2016).
- [126] W. G. F. Krüger, W. Chen, X. Jin, Y. Li, and L. Janssen, *Triple- q Order in $\text{Na}_2\text{Co}_2\text{TeO}_6$ from Proximity to Hidden- $\text{SU}(2)$ -Symmetric Point*, *Phys. Rev. Lett.* **131**, 146702 (2023).
- [127] N. Francini and L. Janssen, *Spin vestigial orders in extended Heisenberg-Kitaev models near hidden $\text{SU}(2)$ points: Application to $\text{Na}_2\text{Co}_2\text{TeO}_6$* , *Phys. Rev. B* **109**, 075104 (2024).
- [128] Y. Gu, X. Li, Y. Chen, K. Iida, A. Nakao, K. Munakata, V. O. Garlea, Y. Li, G. Deng, I. A. Zalitznyak, J. M. Tranquada, and Y. Li, *In-plane multi- q magnetic ground state of $\text{Na}_3\text{Co}_2\text{SbO}_6$* , *Phys. Rev. B* **109**, L060410 (2024).
- [129] N. Metropolis, A. W. Rosenbluth, M. N. Rosenbluth, A. H. Teller, and E. Teller, *Equation of State Calculations by Fast Computing Machines*, *The Journal of Chemical Physics* **21**, 1087 (1953).
- [130] R. H. Swendsen and J.-S. Wang, *Replica Monte Carlo Simulation of Spin-Glasses*, *Phys. Rev. Lett.* **57**, 2607 (1986).
- [131] K. Hukushima and K. Nemoto, *Exchange Monte Carlo Method and Application to Spin Glass Simulations*, *Journal of the Physical Society of Japan* **65**, 1604 (1996).
- [132] D. J. Earl and M. W. Deem, *Parallel tempering: Theory, applications, and new perspectives*, *Phys. Chem. Chem. Phys.* **7**, 3910 (2005).
- [133] E. Hairer, G. Wanner, and S. P. Nørsett, *Solving Ordinary Differential Equations I – Nonstiff Problems* (Springer Berlin Heidelberg, 1993).
- [134] W. H. Press, S. A. Teukolsky, W. T. Vetterling, and B. P. Flannery, *Numerical Recipes 3rd Edition: The Art of Scientific Computing*, 3rd ed. (Cambridge University Press, New York, NY, USA, 2007).
- [135] M. Frigo and S. G. Johnson, *The Design and Implementation of FFTW3*, *Proceedings of the IEEE* **93**, 216 (2005), special issue on “Program Generation, Optimization, and Platform Adaptation”.
- [136] G. B. Arfken and H. J. Weber, *Mathematical Methods for Physicists – International Edition*,

- 4th ed. (Academic Press, INC, 1995).
- [137] S. Zhang, H. J. Changlani, K. W. Plumb, O. Tchernyshyov, and R. Moessner, *Dynamical Structure Factor of the Three-Dimensional Quantum Spin Liquid Candidate NaCaNi₂F₇*, [Phys. Rev. Lett. **122**, 167203 \(2019\)](#).
- [138] C. C. Price and N. B. Perkins, *Critical Properties of the Kitaev-Heisenberg Model*, [Phys. Rev. Lett. **109**, 187201 \(2012\)](#).
- [139] C. Price and N. B. Perkins, *Finite-temperature phase diagram of the classical Kitaev-Heisenberg model*, [Phys. Rev. B **88**, 024410 \(2013\)](#).